

Real-time prediction of plasma instabilities with sparse-grid-accelerated optimized dynamic mode decomposition

Kevin Gill^{a,*}, Ionuț-Gabriel Farcaș^b, Silke Glas^c, Benjamin J. Faber^a

^a*Department of Nuclear Engineering and Engineering Physics, University of Wisconsin–Madison, Madison, WI, 53706, USA*

^b*Department of Mathematics and Division of Computational Modeling and Data Analytics, Academy of Data Science, Virginia Tech, Blacksburg, VA, 24061, USA*

^c*Department of Applied Mathematics, University of Twente, P.O. Box 217, 7500AE Enschede, The Netherlands*

Abstract

Parametric data-driven reduced-order models (ROMs) that embed dependencies in a large number of input parameters are crucial for enabling many-query tasks in large-scale problems. These tasks, including design optimization, control, and uncertainty quantification, are essential for developing digital twins in real-world applications. However, standard training data generation methods are computationally prohibitive due to the curse of dimensionality, as their cost scales exponentially with the number of inputs. This paper investigates efficient training of parametric data-driven ROMs using sparse grid interpolation with (L)-Leja points, specifically targeting scenarios with higher-dimensional input parameter spaces. (L)-Leja points are nested and exhibit slow growth, resulting in sparse grids with low cardinality in low-to-medium dimensional settings, making them ideal for large-scale, computationally expensive problems. Focusing on gyrokinetic simulations of plasma micro-instabilities in fusion experiments as a representative real-world application, we construct parametric ROMs for the full 5D gyrokinetic distribution function via optimized dynamic mode decomposition (optDMD) and sparse grids based on (L)-Leja points. We perform detailed experiments in two scenarios: First, the Cyclone Base Case benchmark assesses optDMD ROM prediction capabilities beyond training time horizons and across variations in the binormal wave number. Second, for a real-world electron temperature gradient driven micro-instability simulation featuring six input parameters, we demonstrate that an accurate parametric optDMD ROM can be constructed at a cost of only 28 high-fidelity gyrokinetic simulations thanks to sparse grids. In the broader context of fusion research, these results demonstrate the potential of sparse grid-based parametric ROMs to enable otherwise intractable many-query tasks.

Keywords: data-driven reduced order modeling, higher-dimensional parameter spaces, sparse grids, optimized dynamic mode decomposition, plasma micro-instability simulations

1. Introduction

High-performance computing (HPC) is crucial for simulating complex real-world phenomena across scientific and engineering disciplines. Today's exascale supercomputers [5] can handle simulations with trillions of degrees of freedom [13], a scale unimaginable just decades ago. Historically, HPC has been used to conduct a single or a small set of forward simulations with predefined input parameters. Yet, addressing practically relevant tasks—such as designing and controlling optimized fusion reactors or performing numerical simulations to support the development of next-generation propulsion devices—requires moving beyond this approach. For tasks like design, control, sensitivity analysis, uncertainty quantification, and solving inverse problems, the cost of performing large ensembles of high-fidelity simulations is prohibitive. Consequently, parametric reduced-order models (ROMs) [9], which embed the variation of key input parameters with the goal of providing computationally cheap approximations, are as important as ever.

*Corresponding author.

Email address: kevin.gill@wisc.edu (Kevin Gill)

This paper focuses on non-intrusive parametric data-driven ROMs with a higher-dimensional parameter space trained from simulation data. This approach is motivated by the complexity of real-world simulation codes, making data-driven methods a convenient way to construct ROMs without needing access to potentially complex or proprietary codebases. Given a set of training parameter instances, parametric ROMs are built using the corresponding high-fidelity simulation data. Once trained, they provide rapid online predictions for arbitrary parameter instances, typically within the same domain as the training parameters. While significant effort has gone into developing new methods for constructing such data-driven parametric ROMs, less emphasis has been placed on efficiently handling high-dimensional parameter spaces. This, in turn, is crucial in practice since the cost of a single high-fidelity simulation can be significant. In this paper, we investigate a sparse grid approach for efficiently constructing parametric ROMs suitable for higher-dimensional parameter spaces and computationally expensive simulation codes. We demonstrate the effectiveness of this approach in a real-world application: the simulation of plasma micro-turbulence in fusion experiments, an area that stands to benefit greatly from parametric ROMs. We note, however, that the ideas investigated in this work are broadly applicable and easily transferable to other application scenarios.

Achieving commercially viable fusion energy hinges on our ability to understand, predict, and control turbulent transport in magnetic confinement devices [91]. In this regard, HPC plays a key role through detailed plasma turbulence simulations, enabling a shift from simpler qualitative descriptions to detailed and quantitative predictions, enabling progress towards full-device [39] and complex multiscale turbulent transport simulations [8]. However, these advanced simulations consume significant resources, limiting the number of cases that can be studied explicitly. This critically underscores the need for innovative parametric reduced-order modeling approaches to enable these otherwise infeasible tasks.

Over the past decades, parametric ROMs have been the subject of extensive research. This body of work encompasses intrusive methods [1, 12, 15, 16, 17, 34, 42, 65, 70, 71] and non-intrusive approaches [2, 22, 50, 67, 74, 75, 80, 90] developed for both linear and nonlinear systems. This also includes more recent extensions based on machine learning approaches [36, 63, 76]. A comprehensive review is available in Ref. [9]. Generally, these methods necessitate acquiring a training dataset, typically from high-fidelity simulations, for a given set of input parameter instances. However, when the number of parameters is large, standard methods for selecting this set of parameter instances become prohibitively expensive due to the curse of dimensionality.

Sparse grids [18] offer a promising approach for combating the curse of dimensionality in higher-dimensional parameter spaces. Essentially, sparse grids construct a multi-dimensional grid by intelligently combining lower-dimensional full tensor product grids, prioritizing grid point combinations that contribute most significantly to overall accuracy of the target approximation. This technique has also found application in model reduction. For instance, Ref. [70] utilized sparse grids, specifically those constructed using standard dyadic grids, with the reduced basis method [65] for constructing reduced basis spaces. Ref. [70] also explored directly interpolating the output of interest on sparse grids to circumvent the reduced basis method entirely. In a similar vein, Ref. [81] used dyadic sparse grids for parametric ROMs of large symmetric linear time-invariant dynamical systems. A non-intrusive reduction method for porous media multiphase flows using Smolyak sparse grids was developed in Ref. [90]. Ref. [92] employed stochastic collocation based on dimension-adaptive sparse grids [40] and projection-based ROMs for optimization problems constrained by partial differential equations (PDEs) with uncertain coefficients. In contrast to existing approaches—which have primarily focused on intrusive reduced modeling, bypassing the ROM construction, or were limited to linear time-invariant systems or specialized applications—we propose integrating sparse grid interpolation based on (L)-Leja points [52, 68] into the parametric ROM construction. This approach is broadly applicable to both linear and nonlinear data-driven parametric reduced modeling. (L)-Leja points can be constructed over arbitrary domains characterized by arbitrary density functions, are arbitrarily granular and form a nested interpolatory sequence (i.e., only one extra point is needed to increase the interpolation degree by one). This means that the cardinality of sparse (L)-Leja grids grows slowly with the dimension, which is desirable for computationally expensive problems. Furthermore, these points were shown to have excellent interpolation accuracy [68]. Here, we will use sparse (L)-Leja grids to generate training data, and interpolation for obtaining parametric ROM predictions for arbitrary input parameter instances.

We will demonstrate the potential of our parametric data-driven reduced modeling approach with (L)-

Leja sparse grids in plasma micro-instability simulations [38]. We model plasma micro-instabilities via the gyrokinetic system of equations [14], which represents perhaps the most widely used approach in practice. Gyrokinetics effectively reduces the plasma phase space from 6D (three positions, three velocities) to 5D (three positions, two velocities) and allows for larger numerical step sizes by averaging over the fast gyromotion of plasma particles. Various simulation approaches exist to solve the gyrokinetic equations [6, 21, 44, 54, 57, 60, 62, 64, 66, 87]. Here, we will use the gyrokinetic code GENE [43, 54], an Eulerian (i.e., grid-based) code that implements one of the most comprehensive physical models for studying micro-instabilities and micro-turbulence. With recent advancements in data-driven modeling and machine learning, there has been a growing interest in surrogate modeling for plasma physics [3, 28, 29, 35, 41, 56, 72, 82], including gyrokinetics [26, 33, 37, 46, 48, 77]. Moreover, sparse grids have been leveraged to efficiently construct surrogate models for the mapping between key input parameters and scalar outputs [30, 31, 33, 58].

Our goal is to extend the existing work and construct parametric data-driven ROMs to quickly and accurately predict the full phase space structure of dominant micro-instability modes in scenarios with a higher-dimensional parameter space. This is achieved by performing linear (in phase space variables) simulations, which are essential for identifying the underlying micro-instabilities. To this aim, we will construct parametric data-driven ROMs based on optimized Dynamic Mode Decomposition (optDMD) [4, 20] using training data computed with GENE. Standard DMD [61, 80, 84] is a data-driven dimensionality reduction technique, developed by Peter Schmid [80], that extracts meaningful spatiotemporal patterns from data. It identifies a set of dynamic modes, each associated with a specific oscillation frequency and a growth or decay rate. DMD seeks to find a best-fit linear operator that maps a data snapshot at one time instant to the next, making it an ideal candidate for modeling linear systems (and beyond, due to its connection to Koopman theory [79]). DMD is often used for analysis, i.e., for understanding the underlying dynamic processes of a system from observed data, as demonstrated in a recent study on mode transition for electromagnetic drift wave instabilities in linear gyrokinetic simulations [26]. However, standard DMD faces challenges such as sensitivity to noise and difficulty in selecting the optimal number of modes for reconstruction. In contrast, optDMD addresses these limitations by recasting the DMD problem as a nonlinear optimization problem to find the optimal set of DMD modes and their corresponding dynamics. Here, we will go beyond conventional analysis as well as surrogate models that map input parameters to scalar outputs. Building upon the pyDMD framework [51], we propose to construct parametric ROMs that integrate optDMD and sparse grid interpolation based on (L)-Leja points for predicting the full phase space structure of dominant micro-instability modes across a wide range of input parameters in fusion plasma scenarios. In a real-world scenario involving electron temperature gradient-driven micro-instability modes at the edge of fusion experiments [25, 54], simulated with GENE in a six-dimensional parameter space, we show that an accurate parametric sparse grid optDMD ROM can be trained using only 28 (L)-Leja points. Our code is available at https://github.com/kevinsinghgil/parametric_ROMs. To our knowledge, this represents one of the first investigations into parametric reduced modeling specifically for gyrokinetic simulations of plasma micro-instabilities. In the broader context of fusion research, parametric ROMs represent a tool for enabling otherwise infeasible tasks such as (design) optimization, control, and uncertainty quantification.

The remainder of this paper is organized as follows. Section 2 provides background on data-driven reduced modeling with parametric variations, optDMD, and sparse grid interpolation using (L)-Leja points. Section 3 summarizes gyrokinetic modeling for plasma micro-instability simulations and the gyrokinetic code GENE. Our approach for constructing parametric data-driven ROMs for higher-dimensional input spaces with optDMD and (L)-Leja sparse grid interpolation is presented in Section 4. Section 5 showcases our findings across two plasma micro-instability simulation scenarios: the Cyclone Base Case benchmark [24], where we investigate optDMD ROMs for forecasting beyond a training time horizon and for variations in a key plasma parameter, and a real-world electron temperature gradient mode simulation with variations in six parameters. Section 6 concludes the paper.

2. Preliminaries

Section 2.1 summarizes the general setup for data-driven parametric reduced modeling. We then provide overviews of optDMD (Sec. 2.2) and sparse grid interpolation with (L)-Leja points (Sec. 2.3), as these

techniques form the building blocks for constructing the parametric ROMs presented in this paper.

2.1. Setup for data-driven reduced-order modeling with parametric variations

This work focuses on learning parametric data-driven ROMs that embed variations in $d \in \mathbb{N}$ input parameters $\boldsymbol{\theta} \in \mathcal{D}$ in a domain $\mathcal{D} \subseteq \mathbb{R}^d$. We specifically target scenarios where the number of parameters, d , is sufficiently large to warrant efficient approaches for generating training data to construct ROMs. Let $[t_i, t_f]$ denote a time interval of interest, with t_i being the initial time and t_f being the final time. We define the complex-valued state vector $\mathbf{g}(t; \boldsymbol{\theta}) = [g_1(t; \boldsymbol{\theta}), g_2(t; \boldsymbol{\theta}), \dots, g_n(t; \boldsymbol{\theta})]^\top \in \mathbb{C}^n$ of dimension $n \in \mathbb{N}$. After spatial discretization, the dynamics of the given problem are generically modeled as a system of nonlinear ordinary differential equations (ODEs), i.e.,

$$\frac{d\mathbf{g}}{dt}(t; \boldsymbol{\theta}) = \mathbf{f}(\mathbf{g}(t; \boldsymbol{\theta}), t; \boldsymbol{\theta}), \quad \mathbf{g}(t_i; \boldsymbol{\theta}) = \mathbf{g}_{\text{init}}(\boldsymbol{\theta}), \quad (1)$$

where $\mathbf{g}_{\text{init}}(\boldsymbol{\theta})$ is a specified initial condition and $\mathbf{f} : \mathbb{C}^n \times [t_i, t_f] \times \mathcal{D} \rightarrow \mathbb{C}^n$ is a (possibly nonlinear) function that defines the time evolution of the system state. The above system of ODEs represents the underlying system of discretized PDEs and the dimension n scales with the dimension of the spatial discretization. In plasma micro-instability and micro-turbulence simulations, for example, n is typically of order 10^5 – 10^9 .

Let $\boldsymbol{\theta}_1, \boldsymbol{\theta}_2, \dots, \boldsymbol{\theta}_{n_p} \in \mathcal{D}$ be $n_p \in \mathbb{N}$ parameter instances and let $\mathbf{g}_k(\boldsymbol{\theta}_j)$ denote the state solution at time t_k for parameter instance $\boldsymbol{\theta}_j$, where we use the notation $\mathbf{g}_k(\boldsymbol{\theta}_j) \equiv \mathbf{g}(t_k; \boldsymbol{\theta}_j)$. We collect $n_t \in \mathbb{N}$ uniformly spaced snapshots over the time domain of interest $[t_i, t_f]$ for each parameter instance $\boldsymbol{\theta}_j$ by solving the high-fidelity model (1) for each $\boldsymbol{\theta}_1, \boldsymbol{\theta}_2, \dots, \boldsymbol{\theta}_{n_p}$ and recording the corresponding solutions at the n_t time instants. Note that we assume that we collect the *same* number of snapshots n_t for each training parameter instance. For a training parameter instance $\boldsymbol{\theta}_j$, we define the trajectory

$$\mathbf{G}_j := [\mathbf{g}_1(\boldsymbol{\theta}_j), \mathbf{g}_2(\boldsymbol{\theta}_j), \dots, \mathbf{g}_{n_t}(\boldsymbol{\theta}_j)] \in \mathbb{C}^{n \times n_t}.$$

In practice, the matrices \mathbf{G}_j are “tall-and-skinny”, i.e., $n \gg n_t$. Given $\mathbf{G}_1, \mathbf{G}_2, \dots, \mathbf{G}_{n_p}$, our goal is to learn parametric data-driven ROMs that provide accurate predictions for an arbitrary $\boldsymbol{\theta} \in \mathcal{D}$.

Several methods exist for constructing parametric ROMs that embed parametric dependence; a comprehensive survey can be found in Ref. [9]. These methods generally differ in how they build the reduced basis and the reduced model operators. When it comes to constructing the reduced basis, approaches typically fall into two categories: those that use local bases (built for each training parameter instance $\boldsymbol{\theta}_1, \boldsymbol{\theta}_2, \dots, \boldsymbol{\theta}_{n_p}$) and those that employ a global reduced basis (constructed from data across all training parameter instances). Similarly, reduced model operators can be built for each individual training parameter instance, or a single set of (global) reduced operators can be constructed. The latter is particularly well-suited for models with an affine dependence on $\boldsymbol{\theta}$. For example, for a linear time-invariant model described by $\frac{d\mathbf{g}}{dt}(t; \boldsymbol{\theta}) = \mathbf{A}(\mathbf{g}; \boldsymbol{\theta})$, an affine structure means that $\mathbf{A}(\mathbf{g}; \boldsymbol{\theta}) = \sum_{k=1}^{q_A} \nu_k(\boldsymbol{\theta}) \mathbf{A}_k(\mathbf{g})$, where q_A is the number of affine terms and $\nu_k(\boldsymbol{\theta})$ are scalar-valued functions such that $\{\nu_k(\boldsymbol{\theta})\}_{k=1}^{q_A}$ is linearly independent. When bases or reduced operators are individually constructed for each training parameter instance, interpolation is commonly used to derive the corresponding reduced basis or operator for any arbitrary $\boldsymbol{\theta} \in \mathcal{D}$. In this work, we compute a global reduced basis using the data for all training parameter instances and use interpolation to compute predictions for an arbitrary $\boldsymbol{\theta} \in \mathcal{D}$. More details are provided in Sec. 4.

2.2. Learning data-driven reduced models with optimized dynamic mode decomposition

This paper focuses on learning parametric ROMs for plasma micro-instability simulations. As these simulations are linear in the phase-space variables, constructing linear ROMs is a natural choice. We therefore leverage optDMD for building parametric ROMs. This section provides a brief overview of standard DMD, followed by a summary of optDMD (for further details, see Refs. [4, 20, 61, 80, 84]). Subsequently, Sec. 4 will detail how optDMD is specifically employed to construct parametric ROMs.

DMD is a data-driven method used to decompose complex system dynamics into a set of spatiotemporal modes, each associated with a fixed oscillation frequency and decay or growth rate. It is particularly effective

for analyzing time-resolved data from simulations or experiments. Assume the parameter of interest is fixed to a value $\boldsymbol{\theta} = \boldsymbol{\theta}_f$. Given a sequence of snapshot measurements $\mathbf{g}_1(\boldsymbol{\theta}_f), \mathbf{g}_2(\boldsymbol{\theta}_f), \dots, \mathbf{g}_{n_t-1}(\boldsymbol{\theta}_f) \in \mathbb{C}^n$, standard DMD seeks to find a best-fit linear operator $\mathbf{A} \equiv \mathbf{A}(\mathbf{g}; \boldsymbol{\theta}_f) \in \mathbb{C}^{n \times n}$ such that $\mathbf{g}_{k+1}(\boldsymbol{\theta}_f) \approx \mathbf{A}\mathbf{g}_k(\boldsymbol{\theta}_f)$. This operator \mathbf{A} maps the system state from one time step to the next. Arranging the snapshot data into the following two shifted matrices $\mathbf{G}^\ell, \mathbf{G}^{\ell+1} \in \mathbb{C}^{n \times (n_t-1)}$,

$$\mathbf{G}^\ell = [\mathbf{g}_1(\boldsymbol{\theta}_f) \quad \mathbf{g}_2(\boldsymbol{\theta}_f) \quad \dots \quad \mathbf{g}_{n_t-1}(\boldsymbol{\theta}_f)], \quad \mathbf{G}^{\ell+1} = [\mathbf{g}_2(\boldsymbol{\theta}_f) \quad \mathbf{g}_3(\boldsymbol{\theta}_f) \quad \dots \quad \mathbf{g}_{n_t}(\boldsymbol{\theta}_f)],$$

the linear operator \mathbf{A} can be approximated by minimizing the Frobenius norm of the residual:

$$\min_{\mathbf{A}} \|\mathbf{G}^{\ell+1} - \mathbf{A}\mathbf{G}^\ell\|_F.$$

The solution to this least-squares problem is $\mathbf{A} = \mathbf{G}^{\ell+1}(\mathbf{G}^\ell)^\dagger$, where $(\mathbf{G}^\ell)^\dagger$ is the Moore-Penrose pseudoinverse of \mathbf{G}^ℓ . In large-scale applications, a low-rank approximation of \mathbf{A} is often computed using the singular value decomposition (SVD) of $\mathbf{G}^\ell = \mathbf{U}\boldsymbol{\Sigma}\mathbf{V}^*$. The DMD modes are then typically computed depending on the eigenvectors of a rank- r projected matrix $\widehat{\mathbf{A}} = \mathbf{U}_r^* \mathbf{A} \mathbf{U}_r = \mathbf{U}_r^* \mathbf{G}^{\ell+1} \mathbf{V}_r \boldsymbol{\Sigma}_r^{-1}$. To simplify the notation, we omit the dependence on $\boldsymbol{\theta}_f$ in the remainder of this section.

Let $\widehat{\boldsymbol{\lambda}} \in \mathbb{C}^r$ denote the eigenvalues of $\widehat{\mathbf{A}}$ and $\widehat{\mathbf{W}} \in \mathbb{C}^{r \times r}$ the corresponding eigenvectors. The DMD modes $\widehat{\boldsymbol{\Phi}} \in \mathbb{C}^{n \times r}$ can be computed as $\widehat{\boldsymbol{\Phi}} = \mathbf{U}_r \widehat{\mathbf{W}}$. A reconstruction of the system dynamics at a time instant t can be expressed as a linear combination of these modes:

$$\mathbf{g}(t) = \widehat{\boldsymbol{\Phi}} \exp(\text{diag}(\widehat{\boldsymbol{\alpha}})t) \widehat{\mathbf{b}},$$

where $\widehat{\boldsymbol{\alpha}}$ denote the continuous time eigenvalues with entries $\alpha_i = \ln(\widehat{\lambda}_i)/\Delta t$ and

$$\widehat{\mathbf{b}} = \widehat{\boldsymbol{\Phi}}^\dagger \mathbf{g}_1 \tag{2}$$

are the mode amplitudes determined from initial conditions.

While standard DMD provides a powerful decomposition, its formulation is based on a least-squares approximation of a linear operator, which does not directly optimize for the accuracy of the reconstructed dynamics. The optDMD [4] addresses this limitation by reformulating the problem as a nonlinear optimization to directly minimize the reconstruction error of the entire time-series data. Instead of directly approximating the operator \mathbf{A} , optDMD seeks to find $\{\widehat{\boldsymbol{\Phi}}, \widehat{\boldsymbol{\alpha}}, \widehat{\mathbf{b}}\}$ that best reconstruct the entire snapshot sequence \mathbf{G} . The optimization problem is typically formulated as:

$$\min_{\widehat{\boldsymbol{\Phi}}, \widehat{\boldsymbol{\alpha}}, \widehat{\mathbf{b}}} \left\| \mathbf{G} - \widehat{\boldsymbol{\Phi}} \text{diag}(\widehat{\mathbf{b}}) \mathbf{M}(\widehat{\boldsymbol{\alpha}}) \right\|_F^2, \tag{3}$$

where \mathbf{G} represents the full snapshot matrix and $\mathbf{M}(\widehat{\boldsymbol{\alpha}}) \in \mathbb{C}^{r \times (n_t)}$ is a matrix with the (i, j) th entry being $\exp(\alpha_i t_j)$, where $t_j = j\Delta t$. Solving this non-convex optimization problem often leads to more accurate and robust reconstructions of the system dynamics compared to standard DMD, particularly when noise is present or when seeking a globally optimal representation of the underlying dynamics. This minimization problem is commonly solved using a Levenberg-Marquardt algorithm, which converges to a (local) optimizer depending on the initial value $\widehat{\boldsymbol{\alpha}}^{(0)}$. In this work, the optDMD procedure is initialized using $\widehat{\boldsymbol{\alpha}}^{(0)} = \ln(\widehat{\boldsymbol{\lambda}}^{(0)})/\Delta t$, where $\widehat{\boldsymbol{\lambda}}^{(0)}$ represent the discrete eigenvalues computed with standard DMD. For its implementation, we employ the pyDMD software package [51], which supports standard DMD, optDMD, and many other variants.

2.3. Sparse grid interpolation using (L)-Leja points

Key to our approach for learning higher-dimensional parametric data-driven ROMs is sparse grid interpolation using (L)-Leja points. In the following, we provide an overview of this method and refer the reader to [30, 32, 52, 68] for more details.

Let $h : \mathcal{X} \subseteq \mathbb{R}^d \rightarrow \mathbb{R}$ denote a multivariate function that is at least continuous on \mathcal{X} . Furthermore, let π denote a multivariate probability density function with support \mathcal{X} . We assume the components of the input $\mathbf{x} \in \mathcal{X}$ to h are independent. This implies that \mathcal{X} and π must have a product structure, i.e., $\mathcal{X} := \bigotimes_{i=1}^d \mathcal{X}_i$ and $\pi(\mathbf{x}) := \prod_{i=1}^d \pi_i(x_i)$, where \mathcal{X}_i is the support of the density π_i associated with input x_i .

Sparse grid interpolation aims to provide a computationally efficient approach for approximating h at an arbitrary $\mathbf{x} \in \mathcal{X}$. This is achieved by forming a linear combination of judiciously selected d -variate products of one-dimensional approximations, formally written as follows:

$$\mathcal{U}_{\mathcal{L}}^d[h] : \mathcal{X} \rightarrow \mathbb{R}, \quad \mathcal{U}_{\mathcal{L}}^d[h](\mathbf{x}) = \sum_{\boldsymbol{\ell} \in \mathcal{L}} \Delta_{\boldsymbol{\ell}}^d[h](\mathbf{x}) = \sum_{\boldsymbol{\ell} \in \mathcal{L}} \sum_{\mathbf{z} \in \{0,1\}^d} (-1)^{|\mathbf{z}|_1} \mathcal{U}_{\boldsymbol{\ell}-\mathbf{z}}^d[h](\mathbf{x}), \quad (4)$$

where $\boldsymbol{\ell} = (\ell_1, \ell_2, \dots, \ell_d) \in \mathbb{N}^d$ denotes a *multiindex*, and $\mathcal{L} \subset \mathbb{N}^d$ is a *multiindex set* defined as

$$\mathcal{L} = \{\boldsymbol{\ell} \in \mathbb{N}^d : |\boldsymbol{\ell}|_1 \leq L + d - 1\}, \quad (5)$$

where $|\boldsymbol{\ell}|_1 = \sum_{i=1}^d \ell_i$ and $L \in \mathbb{N}$ denotes the sparse grid level. The terms $\Delta_{\boldsymbol{\ell}}^d[h](\mathbf{x})$ are known as hierarchical surpluses, derived from full-grid operators, $\mathcal{U}_{\boldsymbol{\ell}}^d$, which are in turn are computed through the tensor product of one-dimensional approximations $\mathcal{U}_{\ell_1}^i, \mathcal{U}_{\ell_2}^i, \dots, \mathcal{U}_{\ell_d}^i$ with support \mathcal{X}_i :

$$\mathcal{U}_{\boldsymbol{\ell}}^d[h](\mathbf{x}) = \left(\bigotimes_{i=1}^d \mathcal{U}_{\ell_i}^i \right) [h](\mathbf{x}),$$

In this work, the one-dimensional approximations, $\mathcal{U}_{\ell_i}^i$, are interpolation approximations based on Lagrange polynomials computed using the (first form of the) barycentric formula for improved numerical stability [10]. A critical aspect for obtaining efficient and accurate interpolation approximations is the choice of interpolation points or knots. Here, we employ (L)-Leja points which were shown to have an excellent interpolation accuracy [68]. Moreover, these points can be constructed over arbitrary domains characterized by arbitrary probability density functions π_i . Let N_i denote the number of 1D (L)-Leja points associated to index ℓ_i . The one-dimensional sequence $\{x_1, x_2, \dots, x_{N_i}\} \sim \pi_i$ of (L)-Leja points is constructed greedily as:

$$x_1 = \operatorname{argmax}_{x \in \mathcal{X}_i} \sqrt{\pi_i(x)}$$

$$x_k = \operatorname{argmax}_{x \in \mathcal{X}_i} \sqrt{\pi_i(x)} \prod_{j=1}^{k-1} |(x - x_j)|, \quad k = 2, 3, \dots, N_i.$$

(L)-Leja points are nested and only one extra point is needed per level to increase the interpolation degree by one. In this case, $N_i = \ell_i$, which we are also using in our experiments. However, since (L)-Leja points are arbitrarily granular, the user has a fine-grained control over their growth beyond this choice.

For a given sparse grid level L , the multivariate interpolation approximation (4) is obtained using N data pairs $\{(\mathbf{x}_j, h(\mathbf{x}_j))\}_{j=1}^N$, where N denotes the total number of multivariate (L)-Leja points associated with the multiindex set \mathcal{L} defined in Eq. (5). N is significantly smaller than the cardinality of the corresponding full-tensor grid, comprising $\prod_{i=1}^d N_i$ points. This is shown in Fig. 1, which compares the cardinality of a sparse (L)-Leja grid to that of the corresponding full tensor grid for $d \in \{2, 4, 6, 8, 10\}$ and $L \in \{2, 3, 4, 5\}$.

3. Gyrokinetic plasma micro-instability and micro-turbulence simulations

As a representative real-world application poised to benefit from parametric data-driven reduced modeling, we consider the simulation of plasma micro-instabilities in fusion experiments [38]. Section 3.1 summarizes gyrokinetic modeling for plasma micro-instability simulations and Section 3.2 presents the gyrokinetic code GENE used to generate the high-fidelity training datasets for developing parametric ROMs.

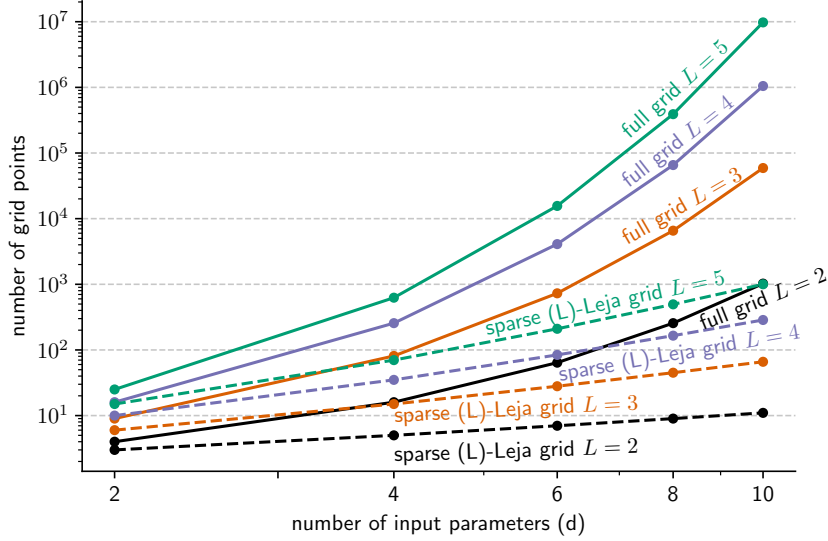


Figure 1: Cardinality of sparse (L)-Leja grids vs. corresponding full tensor grid for $d \in \{2, 4, 6, 8, 10\}$ and level $L \in \{2, 3, 4, 5\}$.

3.1. Gyrokinetic modeling for plasma micro-instability and micro-turbulence simulations

Perhaps the most widely used approach for simulating plasma micro-instabilities and micro-turbulence in practice is the gyrokinetic approach [14], where a 5D plasma phase space distribution function $g_s(\mathbf{X}, v_{\parallel}, \mu, t)$ for each plasma species s is evolved in time and coupled self-consistently with external and internally generated electromagnetic fields via the coupled Vlasov-Maxwell system of PDEs. Here, \mathbf{X} is the gyrocenter position, v_{\parallel} is the velocity component parallel to the background magnetic field $\mathbf{B} = B\mathbf{b}$, and μ is the magnetic moment (a conserved quantity in the collisionless limit). Gyrokinetics provides a good balance between the amount of incorporated physics and their potential to be transformed into predictive high-fidelity numerical models that can be simulated on present computing resources. For most of plasma turbulence applications in magnetically-confined fusion plasmas, the relation $g_{1,s}/g_{0,s} \ll 1$ is satisfied, where $g_{1,s}$ denotes the *fluctuating* distribution function and $g_{0,s}$ is a background (typically a static Maxwellian) distribution such that $g_s = g_{0,s} + g_{1,s}$ and $\langle g_{0,s} \rangle = 0$ for some appropriate spatio-temporal averaging operator $\langle \cdot \rangle$. Thus many of the important properties, such as micro-instability and transport, can be examined by simulating only the evolution of $g_{1,s}$.

The dynamics of plasma species s are governed by the following phase-space conservation equation:

$$\frac{\partial g_s}{\partial t} + \dot{\mathbf{X}} \cdot \nabla g_s + \dot{v}_{\parallel} \frac{\partial g_s}{\partial v_{\parallel}} = \sum_{s'} \mathcal{C}(g_s, g_{s'}). \quad (6)$$

$\mathcal{C}(g_s, g_{s'})$ denotes a collision operation describing inter- and intra-species interactions. The equations of motion for the gyrocenter of a particle with mass m and charge q read

$$\dot{\mathbf{X}} = v_{\parallel} \mathbf{b} + \frac{B}{B_{\parallel}^*} (\mathbf{v}_{\nabla B} + \mathbf{v}_{\kappa} + \mathbf{v}_E), \quad \dot{v}_{\parallel} = -\frac{\dot{\mathbf{X}}}{mv_{\parallel}} \cdot (\mu \nabla B + q \nabla \bar{\phi}) - \frac{q}{m} \dot{A}_{\parallel},$$

where $\mathbf{v}_{\nabla B} = (\mu/(m\Omega B)) \mathbf{B} \times \nabla B$ is the grad-B drift velocity, $\mathbf{v}_{\kappa} = (v_{\parallel}^2/\Omega) (\nabla \times \mathbf{b})_{\perp}$ is the curvature drift velocity, and $\mathbf{v}_E = (1/B^2) \mathbf{B} \times \nabla(\bar{\phi} - v_{\parallel} \bar{A}_{\parallel})$ is the generalized $\mathbf{E} \times \mathbf{B}$ drift velocity. $\Omega = qB/m$ denotes the gyrofrequency and B_{\parallel}^* is the parallel component of the effective magnetic field $\mathbf{B}^* = \mathbf{B} + \frac{B}{\Omega} v_{\parallel} \nabla \times \mathbf{b} + \nabla \times (\mathbf{b} \bar{A}_{\parallel})$. In all of the above expressions, $\bar{\phi}$ and \bar{A}_{\parallel} denote the gyroaveraged versions of the fluctuating electrostatic potential and the parallel component of the vector potential, which are self-consistently computed from the

fluctuating distribution function. Assuming a static background distribution function $g_{0,s}(\mathbf{X}, v_{\parallel}, \mu)$, which allows for the decomposition $g_s(\mathbf{X}, v_{\parallel}, \mu, t) = g_{0,s}(\mathbf{X}, v_{\parallel}, \mu) + g_{1,s}(\mathbf{X}, v_{\parallel}, \mu, t)$, ϕ can be calculated via the Poisson equation, which, expressed at the particle position \mathbf{x} , reads

$$\nabla_{\perp}^2 \phi(\mathbf{x}) = -\frac{1}{\epsilon_0} \sum_s q_s n_{1,s}(\mathbf{x}) = -\frac{1}{\epsilon_0} \sum_s \frac{2\pi q_s}{m_s} \int B_{\parallel}^* g_{1,s}(\mathbf{x}, v_{\parallel}, \mu) dv_{\parallel} d\mu.$$

A_{\parallel} is obtained by solving the parallel component of Ampère's law for the fluctuating fields:

$$-\nabla_{\perp}^2 A_{\parallel}(\mathbf{x}) = \mu_0 \sum_s j_{\parallel,s}(\mathbf{x}) = \mu_0 \sum_s \frac{2\pi q_s}{m_s} \int B_{\parallel}^* v_{\parallel} g_{1,s}(\mathbf{x}, v_{\parallel}, \mu) dv_{\parallel} d\mu.$$

Expressions for connecting $g_s(\mathbf{X}, v_{\parallel}, \mu)$ and $g_s(\mathbf{x}, v_{\parallel}, \mu)$ can be found in the literature [14]. Note that in these formulas, the time dependence has been suppressed for simplicity.

3.2. The gyrokinetic code GENE

To perform high-fidelity gyrokinetic plasma micro-turbulence simulations and generate data for training parametric ROMs, we will use the plasma micro-instability and micro-turbulence simulation code GENE¹ [43, 54]. GENE has been among the first gyrokinetic codes to leverage an Eulerian (i.e., grid-based) representation of the plasma species distributions, thus mitigating the problem of numerical noise affecting codes based on the alternative particle-in-cell approach. GENE uses a method-of-lines approach to reduce the nonlinear integro-differential gyrokinetic equations to a set of ODEs. In this approach, the distribution functions for all the particle species characterizing the plasma are evolved on a fixed grid in the underlying 5D phase space. Periodic boundary conditions are used for both perpendicular directions x and y , which are therefore numerically implemented with spectral methods. We denote by n_{k_x} and n_{k_y} the corresponding number of Fourier modes. The total grid size is $n_{k_x} \times n_{k_y} \times n_z \times n_{v_{\parallel}} \times n_{\mu} \times n_s$, where n_z denotes the number of points in the z direction, and $n_{v_{\parallel}}$ n_{μ} denote the number of grid points used to discretize the velocity space. Moreover, n_s denotes the number of plasma species. GENE employs a coordinate system that is aligned to the background magnetic field in configuration space to allow for an efficient representation of the turbulent fields. This is because the turbulent fluctuations are typically field-aligned with large correlation lengths along the field lines due to parallel streaming, but are typically constrained to correlation lengths on the order of the gyroradius in the perpendicular directions. Furthermore, block-structured grids are adopted to optimally discretize the velocity space [53]. These methods are implemented numerically through an MPI-based domain decomposition approach and achieves excellent performance over thousands of nodes [43]. Recently, GENE has been extended to efficiently utilize GPU hardware to accelerate computationally intensive kernels, again achieving excellent performance over hundreds of nodes [39].

GENE currently implements one of the most comprehensive physical models for studying micro-turbulence: nonlinear kinetic dynamics for an arbitrary number of ion species (including impurities) and electrons, electrostatic and electromagnetic fluctuation fields, interfaces with magnetohydrodynamics (MHD) codes for providing realistic magnetic equilibria [89], as well as inter- and intra-species collision operators [23].

In the present paper, we employ the *local* version of GENE [54], which implements a standard flux-tube model [7], that is, it considers only a sub-volume of the core plasma centered around a particular magnetic field line. While these simulations retain full dependence of the magnetic geometry along the magnetic field line, the radial dependence of background quantities is determined from a first-order Taylor expansion. Thus the flux-tube domains do not incorporate the full radial dependence of either the temperature and density profiles or the magnetic geometry. However, they are well-suited to study local instability and turbulence phenomena in fusion plasmas, such as gyro-radius scale drift wave instabilities, due to the highly anisotropic nature of field-aligned fluctuations. A mixture of finite differences and pseudo-spectral methods are employed to discretize the configuration space, while collisions are incorporated using finite volume methods. The time evolution of the spatially discretized operators is performed using an adaptive fourth-order Runge-Kutta (RK4) time integrator.

¹<http://genecode.org>

4. Learning higher-dimensional parametric data-driven reduced models using sparse grids

This section details our approach for learning higher-dimensional parametric ROMs based on optDMD and sparse grid interpolation with (L)-Leja points. Section 4.1 summarizes the high-fidelity simulation setup, while Section 4.2 describes the construction of parametric ROMs using the aforementioned techniques for linear plasma micro-instability simulations.

4.1. Setup for high-fidelity linear plasma micro-instability simulations

As a real-world example that can benefit from parametric reduced modeling, this paper focuses on constructing data-driven ROMs to quickly and accurately predict the full phase space structure of dominant micro-instability modes in fusion plasma scenarios with high-dimensional input parameter spaces. Specifically, we consider linear, local, flux-tube gyrokinetic simulations with one plasma species (i.e., $n_s = 1$). In linear simulations, $n_{k_y} = 1$. These linear simulations are essential for identifying underlying micro-instabilities, such as ion or electron temperature gradient (ITG/ETG) driven modes, trapped electron modes (TEMs), and micro-tearing modes (MTMs), which form the foundation for nonlinear transport analysis in magnetically confined fusion plasmas. Linear instability characteristics, such as linear growth rates, propagation frequencies and eigenmode structures, provide critical information on the underlying sources of free energy that drives unwanted turbulent transport. These instabilities have complicated dispersion relations that often require numerical simulation to understand, with nontrivial and often nonlinear dependencies on parameters such as wavelength, plasma pressure profiles, and magnetic field structure. Furthermore, establishing their threshold values and transitions in parameter space is particularly useful, as it often informs the selection of input parameters for more complex nonlinear simulations. To this aim, the ROM predictions will include the complex eigenvalue that provides the growth rate and frequency of the unstable, dominant eigenmode (the remaining eigenvalues correspond to stable modes when the ROM reduced dimension $r > 1$) and the time evolution of the distribution function over a target time horizon $[t_i, t_f]$ over the micro-instability saturated phase. The latter can be used to derive other relevant quantities such as the electrostatic potential ϕ , the parallel component of the vector potential A_{\parallel} , and the parallel component of the effective magnetic field B_{\parallel}^* along the magnetic field direction z , defined in Sec. 3.1.

The training data for constructing parametric data-driven ROMs will be generated using the linear initial value solver provided by GENE. In this approach, the nonlinear terms in Eq. (6) are neglected, allowing the governing equations to be compactly written as:

$$\frac{d\mathbf{g}}{dt}(t; \boldsymbol{\theta}) = \mathbf{A}\mathbf{g}(t; \boldsymbol{\theta}), \quad (7)$$

where $\mathbf{A} \in \mathbb{C}^{n \times n}$ and $\mathbf{g}(t; \boldsymbol{\theta}) \in \mathbb{C}^n$ denotes the semi-discrete form of the distribution function for the underlying plasma species. The system is advanced in time using the RK4 time integrator, starting from an initial random distribution function. After an initial transient phase, the growth rate of the distribution function will asymptote to that of the fastest growing instability. The simulation then terminates when the relative change in the running average of this growth rate drops below 10^{-3} , a tolerance typically sufficient in practice. In these simulations, the time domain of interest, $[t_i, t_f]$, is measured in units L_{ref}/c_s , where L_{ref} is the reference length scale and c_s is the ion sound speed.

We will also analyze the full spectrum of the reduced linear operators generated by our ROMs, particularly when the reduced dimension $r > 1$. To this aim, we can employ the GENE linear eigenvalue solver [55] to compute the spectrum for the reference data. In this solver, an iterative Jacobi-Davidson solver with additive Schwarz preconditioning from the SLEPc library [49, 78] is applied to a matrix-free representation of the left side of Eq. 6. A shift parameter for shift-and-invert preconditioning may also be utilized to accelerate convergence in a particular region of the spectrum. The stopping criterion for these eigenvalue calculations requires the eigenvalue residuals be less than 10^{-8} for each eigenvalue/eigenvector pair. Using eigenvalue calculations to study the subdominant and stable eigenmode spectrum is critical to understanding the complex nonlinear dynamics of tokamaks [47, 88] and stellarators [27, 73].

Two different instability scenarios are examined in this paper, one focusing on ITG modes and the other on ETG modes. In both cases, simulations are performed by considering only gyrokinetic ions (electrons)

for the ITG (ETG) parameter set, while the other plasma species are considered “adiabatic” [54]. We note that while a single gyrokinetic species simulation inherently has limiting assumptions, it remains physically relevant. The ITG is expected to be a major limiting factor in plasma performance in fusion scenarios, and has recently been shown to limit performance of the W7-X stellarator [11]. Similarly, the ETG is expected to play a critical role in determining the performance of the tokamak pedestal [86], which is crucial to achieving high performance in tokamaks [85]. Both of these instabilities can be efficiently simulated by using only a single gyrokinetic species, which substantially reduces the cost required for the application presented here. Nevertheless, the phase space states for these simulations are still complex and predicting the full 5D phase space is a nontrivial task. Our future research will extend this methodology to nonlinear gyrokinetic simulations of turbulent transport. This is a highly nontrivial undertaking due to the significantly larger scale, high computational cost, and inherent complexities of their nonlinear and chaotic dynamics.

4.2. Learning higher-dimensional parametric reduced models using (L)-Leja sparse grid interpolation

The strategy for selecting the n_p training parameter instances, $\boldsymbol{\theta}_1, \boldsymbol{\theta}_2, \dots, \boldsymbol{\theta}_{n_p} \in \mathcal{D}$, is critical for efficiently constructing parametric ROMs. In this work, we propose employing sparse grids constructed using (L)-Leja points, as presented in Sec. 2.3, which are ideally suited for problems with higher-dimensional parameter spaces and computationally expensive high-fidelity models. To construct parametric (sparse grid) ROMs, we employ optDMD as summarized in Sec. 2.2. We note that we employ optDMD as a building block for constructing parametric ROMs primarily because our target plasma micro-instability scenarios are linear in the phase-space variables. However, the presented methodology can be extended to ROM approaches targeting nonlinear systems, such as Operator Inference [59, 69].

Let L denote a user-defined sparse grid level with $N = n_p$ parameter instances. Based on our experience, a low grid level (e.g., $L = 3, 4$) is generally sufficient when the target function to be interpolated is smooth. Note that since these grids are nested, increasing the level, if necessary, allows for the reuse of evaluations from previous grid levels. For each of the n_p sparse grid training parameter instances $\boldsymbol{\theta}_1, \boldsymbol{\theta}_2, \dots, \boldsymbol{\theta}_{n_p} \in \mathcal{D}$, we perform the corresponding high-fidelity gyrokinetic simulation using GENE and collect the distribution function at n_t time instants during the micro-instability saturated phase. Each 5D distribution function at a particular time instant is flattened into a column vector of size $n = n_{k_x} \times 1 \times n_z \times n_{v_{\parallel}} \times n_{\mu}$; subsequently, for each training parameter $\boldsymbol{\theta}_j$, these n_t snapshots are compiled into a complex-valued matrix $\mathbf{G}_j \in \mathbb{C}^{n \times n_t}$.

We next use $\mathbf{G}_1, \mathbf{G}_2, \dots, \mathbf{G}_{n_p}$ to compute the global rank- r POD basis. This is done by first stacking the distribution function data horizontally into a snapshot matrix $\mathbf{G} = [\mathbf{G}_1 \ \mathbf{G}_2 \ \dots \ \mathbf{G}_{n_p}] \in \mathbb{C}^{n \times n_p n_t}$ followed by computing its thin SVD,

$$\mathbf{G} = \mathbf{U}\boldsymbol{\Sigma}\mathbf{V}^*,$$

where $\mathbf{U} \in \mathbb{C}^{n \times n_p n_t}$ has unitary columns and contains the left singular vectors, $\boldsymbol{\Sigma} \in \mathbb{R}^{n_p n_t \times n_p n_t}$ is a diagonal matrix containing the singular values of \mathbf{G} in non-decreasing order $\sigma_1 \geq \sigma_2 \geq \dots \geq \sigma_{n_p n_t} \geq 0$, where σ_j denotes the j th singular value, and $\mathbf{V} \in \mathbb{C}^{n_p n_t \times n_p n_t}$ has unitary rows and contains the right singular vectors. The first $r \ll n$ columns of \mathbf{U} , i.e., the left singular vectors corresponding to the r largest singular values, form the POD basis $\mathbf{U}_r \in \mathbb{C}^{n \times r}$. The reduced dimension r can be prescribed a-priori or chosen based on an energy criterion such as

$$\frac{\sum_{i=1}^r \sigma_i^2}{\sum_{i=1}^{n_p n_t} \sigma_i^2} \geq E\%,$$

where $E\%$ is a user-specified energy truncation threshold (e.g., $E\% = 99.99\%$).

Since one goal of parametric ROMs in the present paper is to predict the eigenvalue of the dominant micro-instability mode, we use \mathbf{U}_r and optDMD to directly compute the spectra of the reduced operators $\hat{\mathbf{A}}_1, \hat{\mathbf{A}}_2, \dots, \hat{\mathbf{A}}_{n_p} \in \mathbb{C}^{r \times r}$ along with the reduced initial conditions. This is achieved by leveraging the pyDMD package [51]. These linear reduced operators and corresponding initial conditions describe linear ROMs for the high-fidelity gyrokinetic model (7) for each $\boldsymbol{\theta}_j, j = 1, 2, \dots, n_p$. Note that the reduced linear operators can be trivially computed using their spectra.

The optDMD procedure is initialized with the continuous-time eigenvalues

$$\widehat{\boldsymbol{\alpha}}_j^{(0)} = \left[\widehat{\alpha}_{1,j}^{(0)} \widehat{\alpha}_{2,j}^{(0)} \cdots \widehat{\alpha}_{r,j}^{(0)} \right] = \left[\frac{\ln \left(\widehat{\lambda}_{1,j}^{(0)} \right)}{\Delta t} \frac{\ln \left(\widehat{\lambda}_{2,j}^{(0)} \right)}{\Delta t} \cdots \frac{\ln \left(\widehat{\lambda}_{r,j}^{(0)} \right)}{\Delta t} \right] \in \mathbb{C}^r,$$

where $\left\{ \widehat{\lambda}_{i,j}^{(0)} \right\}_{i=0}^r$ denote the discrete eigenvalues computed with standard DMD and Δt is the uniform sampling interval. The optDMD algorithm computes the r reduced continuous-time eigenvalues $\widehat{\boldsymbol{\alpha}}_j = \left[\widehat{\alpha}_{1,j} \widehat{\alpha}_{2,j} \cdots \widehat{\alpha}_{r,j} \right] \in \mathbb{C}^r$, r optDMD modes $\widehat{\boldsymbol{\Phi}}_j \in \mathbb{C}^{n \times r}$, and r reduced amplitudes (i.e., initial conditions) $\widehat{\mathbf{b}}_j \in \mathbb{R}^r$ for $j = 1, 2, \dots, n_p$. The eigenvectors of $\widehat{\mathbf{A}}_j$ are computed as $\widehat{\mathbf{W}}_j = \mathbf{U}_r^* \widehat{\boldsymbol{\Phi}}_j \in \mathbb{C}^{r \times r}$.

In the next step, we use $\left\{ \widehat{\boldsymbol{\alpha}}_j, \widehat{\mathbf{W}}_j, \widehat{\mathbf{b}}_j \right\}_{j=1}^{n_p}$ to compute predictions for an arbitrary $\boldsymbol{\theta}^\ddagger \in \mathcal{D}$ beyond training. To this end, we interpolate the pairs $\left\{ (\boldsymbol{\theta}_j, \widehat{\boldsymbol{\alpha}}_j) \right\}_{j=1}^{n_p}$, $\left\{ (\boldsymbol{\theta}_j, \widehat{\mathbf{W}}_j) \right\}_{j=1}^{n_p}$, and $\left\{ (\boldsymbol{\theta}_j, \widehat{\mathbf{b}}_j) \right\}_{j=1}^{n_p}$ using sparse grid Lagrange interpolation with (L)-Leja points as described in Sec. 2.3. For a given $\boldsymbol{\theta}^\ddagger \in \mathcal{D}$, this yields $\left\{ \widetilde{\boldsymbol{\alpha}}(\boldsymbol{\theta}^\ddagger), \widetilde{\mathbf{W}}(\boldsymbol{\theta}^\ddagger), \widetilde{\mathbf{b}}(\boldsymbol{\theta}^\ddagger) \right\}$, where $\widetilde{\boldsymbol{\alpha}}(\boldsymbol{\theta}^\ddagger) = \mathcal{U}_{\mathcal{L}}^d[\widehat{\boldsymbol{\alpha}}](\boldsymbol{\theta}^\ddagger)$, $\widetilde{\mathbf{W}}(\boldsymbol{\theta}^\ddagger) = \mathcal{U}_{\mathcal{L}}^d[\widehat{\mathbf{W}}](\boldsymbol{\theta}^\ddagger)$, $\widetilde{\mathbf{b}}(\boldsymbol{\theta}^\ddagger) = \mathcal{U}_{\mathcal{L}}^d[\widehat{\mathbf{b}}](\boldsymbol{\theta}^\ddagger)$, and \mathcal{L} denotes the multiindex set (5) for the given sparse grid level L . The first complex eigenvalue in $\widetilde{\boldsymbol{\alpha}}(\boldsymbol{\theta}^\ddagger)$ provides the growth rate and frequency of the dominant eigenmode; when $r > 1$, the remaining eigenvalues correspond to stable micro-instability modes. The interpolated data $\left\{ \widetilde{\boldsymbol{\alpha}}(\boldsymbol{\theta}^\ddagger), \widetilde{\mathbf{W}}(\boldsymbol{\theta}^\ddagger), \widetilde{\mathbf{b}}(\boldsymbol{\theta}^\ddagger) \right\}$ can be also used to predict the time evolution of the distribution function $\mathbf{g}(t; \boldsymbol{\theta}^\ddagger)$ over the target time horizon $[t_i, t_f]$. More specifically, we compute $\widetilde{\mathbf{g}}(t; \boldsymbol{\theta}^\ddagger) \approx \mathbf{g}(t; \boldsymbol{\theta}^\ddagger)$ at a time instant $t \in [t_i, t_f]$ as

$$\mathbf{g}(t; \boldsymbol{\theta}^\ddagger) \approx \widetilde{\mathbf{g}}(t; \boldsymbol{\theta}^\ddagger) = \widetilde{\boldsymbol{\Phi}}(\boldsymbol{\theta}^\ddagger) \exp(\text{diag}(\widetilde{\boldsymbol{\alpha}}(\boldsymbol{\theta}^\ddagger))t) \widetilde{\mathbf{b}}(\boldsymbol{\theta}^\ddagger) \in \mathbb{C}^n,$$

where $\widetilde{\boldsymbol{\Phi}}(\boldsymbol{\theta}^\ddagger) = \mathbf{U}_r \widetilde{\mathbf{W}}(\boldsymbol{\theta}^\ddagger) \in \mathbb{C}^{n \times r}$ denotes the full-space DMD modes. The prediction of the distribution function can be then used to derive other relevant quantities.

We note that interpolating eigenpairs to obtain predictions for arbitrary parameter instances was also considered in Ref. [50]. However, Ref. [50] used standard DMD to find $\widehat{\mathbf{A}}$ followed by its eigendecomposition, whereas here we employ optDMD to directly compute the eigenpairs as discussed above. Furthermore, Ref. [50] used nearest neighbors to select parameter instances for interpolation, which is affected by the curse of dimensionality, while our approach delays it via sparse grid interpolation, making it suitable for higher-dimensional parametric scenarios. Finally, we use a global reduced basis instead of local bases as in Ref. [50]. Our code is publicly available at https://github.com/kevinsinghgil/parametric_ROMs and is suitable for parametric data-driven reduced modeling beyond linear plasma micro-instability simulations.

Remark 1. *Sparse grid approximations are designed for problems with at least two parameters, i.e., $d \geq 2$. When dealing with a single input parameter, $\boldsymbol{\theta} \in \mathcal{D} \subseteq \mathbb{R}$, we can generate training instances $\boldsymbol{\theta}_1, \boldsymbol{\theta}_2, \dots, \boldsymbol{\theta}_{n_p}$ using standard strategies such as a uniform grid or pseudo-random sampling. Interpolation can then be performed using well-known methods like spline interpolation.*

Remark 2. *While the cardinality of (L)-Leja sparse grids grows slowly with the number of parameters and grid level, it can still become prohibitively large for computationally expensive problems when the dimensionality (d) or sparse grid level (L) are large. One approach to mitigate this is adaptivity, which has proven efficient in high-dimensional problems [31]. We plan to integrate adaptivity into our parametric reduced modeling procedure in future research.*

5. Numerical experiments in two plasma micro-instability simulation scenarios

This section presents our numerical results in two plasma micro-instability simulation scenarios. Section 5.1 examines the Cyclone Base Case (CBC) benchmark, characterized by ITG micro-instability modes. Here, we assess the predictive capabilities of optDMD ROMs in two ways: extrapolating predictions beyond the training period for fixed input parameters, and for variations in one key parameter, the binormal wave number, $k_y \rho_s$. Section 5.2 then explores a real-world scenario: ETG-driven micro-instability in the pedestal

region of a tokamak. We evaluate the efficiency and predictive power of sparse grid-based parametric optDMD ROMs under variations in six key plasma parameters. To our knowledge, this work represents one of the first investigations into parametric reduced modeling for gyrokinetic simulations of plasma micro-instability.

Both the high-fidelity and reduced modeling computations were performed on the Perlmutter supercomputer² at the National Energy Research Scientific Computing Center (NERSC). Each CPU and GPU node is equipped with two AMD EPYC 7763 (Milan) CPUs with 64 cores per CPU and 512 Gb DDR4 memory total. The high-fidelity GENE simulations to generate training and reference data for our ROMs were performed on a single Perlmutter compute node utilizing four NVIDIA A100 GPUs with 80 Gb on-card memory each, linked via GPU-aware MPI. All reduced modeling computations and GENE eigenvalue calculations were performed on one Perlmutter CPU node.

5.1. Cyclone Base Case benchmark with deuterium ions and ion temperature gradient driven modes

We begin by examining the CBC benchmark scenario presented in [24]. We consider a setup with a single plasma species, namely deuterium ions, characterized by ITG micro-instabilities. The electrons are assumed to be adiabatic. For the magnetic geometry, this setup utilizes an s - α circular model. The high-fidelity model is discretized using grid with $n = n_{k_x} \times 1 \times n_z \times n_{v_{\parallel}} \times n_{\mu} = 15 \times 1 \times 16 \times 32 \times 8 = 61,440$ degrees of freedom in the five-dimensional position-velocity phase space.

5.1.1. Reduced-order modeling predictions beyond a training time horizon for fixed parameter values

Setup for reduced-order modeling. In our first set of experiments, we investigate optDMD ROMs for predicting plasma behavior beyond a training time horizon for a fixed set of input parameters. We furthermore assess the prediction capabilities of standard DMD and optDMD. Predictive ROMs are particularly useful for computing long-term predictions that remain computationally too expensive in terms of the high-fidelity simulation model. Specifically, given data over a training horizon $[t_i, t_i]$, the ROM predicts the time evolution of the distribution function over $[t_i, t_f]$, where $t_i < t_f$. Here, we focus on a CBC simulation with $k_y \rho_s = 0.30$, corresponding to ITG-driven micro-instability.

The high-fidelity GENE initial-value simulation is performed over the time domain $[0, 32.993]$ measured in units R/c_s , where R is the major radius of the toroidal plasma. The GENE runtime is 125.154 seconds using four GPUs on a single GPU node on Perlmutter. We save the complex-valued distribution function to disk every 100 time iterations. We explore two setups for constructing linear ROMs for forecasting beyond training. The first setup begins the training horizon during the transient phase, that is, at $t_i = 6.6$. The training horizon ends at $t_t = 19.8$ for a total of $n_t = 132$ training snapshots. Therefore, $\mathbf{G} \in \mathbb{C}^{61,440 \times 132}$. This is generally the preferred approach in practice. Due to the transient nature of subdominant plasma micro-instabilities, practitioners are typically interested only in final dominant micro-instability. However, for a more comprehensive analysis, we also consider a more challenging setup. This alternative approach begins training at $t_i = 0$, thereby including the transient phase, and ends at $t_t = 13.201$, utilizing $n_t = 199$ snapshots for training, which means that $\mathbf{G} \in \mathbb{C}^{61,440 \times 199}$.

Reduced-order modeling predictions beyond the training horizon. Figure 2 plots the singular values (left) and the corresponding retained energy (right) for both considered setups. As expected for a simulation dominated by a single micro-instability mode, the first mode captures the majority of the energy in both cases. Furthermore, the singular values decay rapidly. For the first setup, over 99% of the total energy is contained within the first mode, while for the second setup, this is achieved by the first two modes. Consequently, we construct optDMD ROMs with reduced dimensions $r = 1$ and $r = 2$, respectively.

Figures 3 and 4 illustrate the performance of the optDMD ROM predictions against reference GENE data. These figures compare the expectation of the real (left) and imaginary (right) components of the distribution function across their respective time horizons. Figure 3 further compares predictions from standard DMD and optDMD for the setup where the training horizon begins after the transient phase ($t_i = 6.6$). The standard DMD predictions deviate from the reference results, particularly towards the end of

²<https://docs.nersc.gov/systems/perlmutter/architecture/>

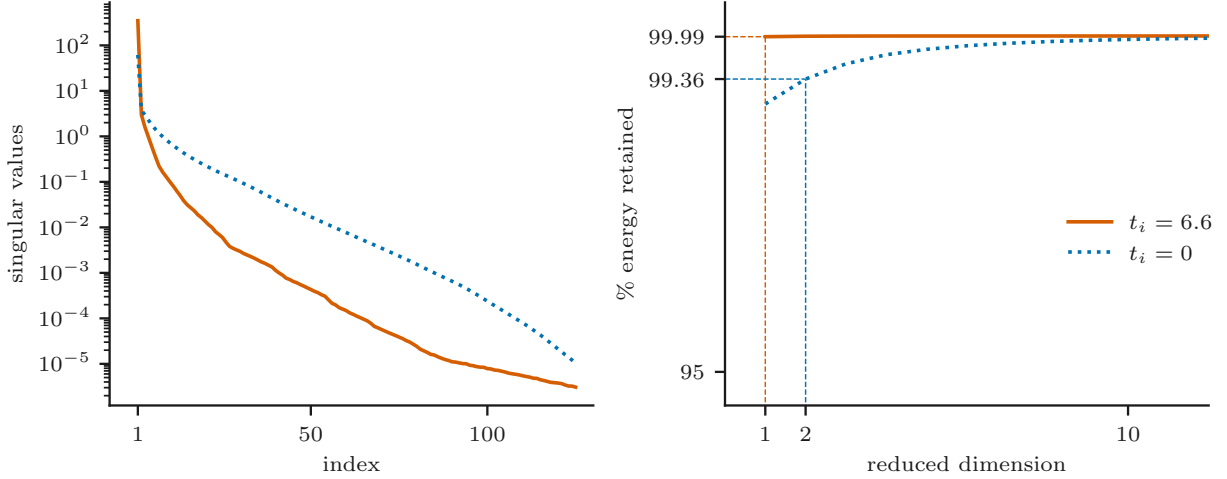


Figure 2: Cyclone Base Case benchmark scenario: Singular values (left) and corresponding retained energy (right) when constructing an optDMD ROM for predictions beyond the training horizon. Orange denotes the case where training horizon begins at $t_i = 6.6$, after the transient phase, and blue denotes the case where the training horizon begins at $t_i = 0$, which includes the transient phase.

the training horizon, which worsens during the prediction horizon. In contrast, optDMD maintains high accuracy across both training and prediction horizons. These findings demonstrate the superior performance of optDMD for ROM-based predictions in our experiments. Despite these differences in predictive accuracy, both standard and optDMD approaches accurately estimate the eigenvalue corresponding to the dominant eigenmode for analysis purposes, a finding consistent with existing literature (e.g., [26]). Specifically, we obtained $\alpha_{\text{ROM}} = 0.263 + 0.789i$ with standard DMD and $\alpha_{\text{ROM}} = 0.263 + 0.790i$ with optDMD. Both values are in excellent agreement with the GENE reference result $\alpha_{\text{ref}} = 0.264 + 0.790i$.

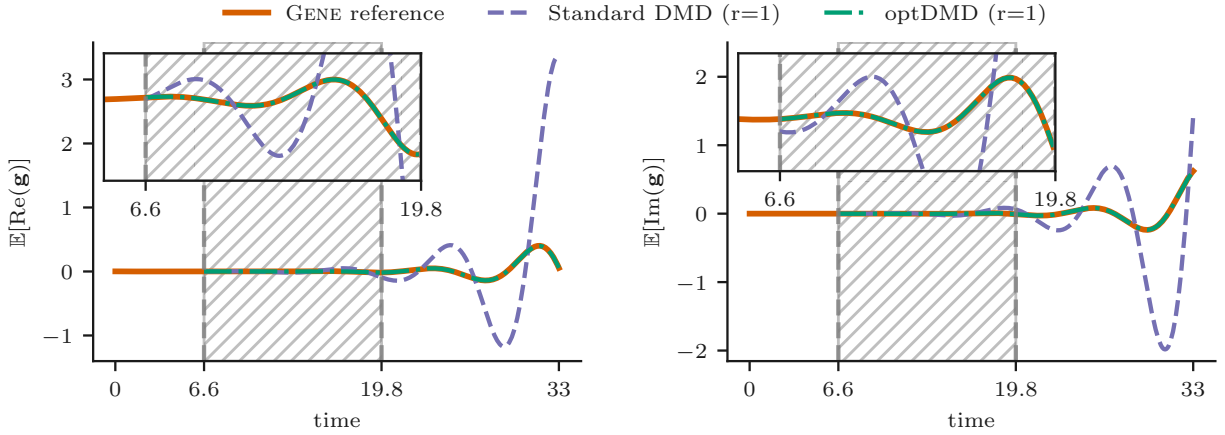


Figure 3: Cyclone Base Case benchmark scenario: Comparison between standard DMD and optDMD for time prediction scenarios shown for test case $k_y \rho_s = 0.30$. The training horizon $[6.6, 19.8]$ is after the transient phase.

Figure 4 plots the optDMD predictions for the more challenging scenario where training begins at $t_i = 0$. Even in this case, the ROM provides accurate predictions; minor discrepancies at the beginning of the time domain are attributed to the intricate transient dynamics. Furthermore, the optDMD ROMs accurately

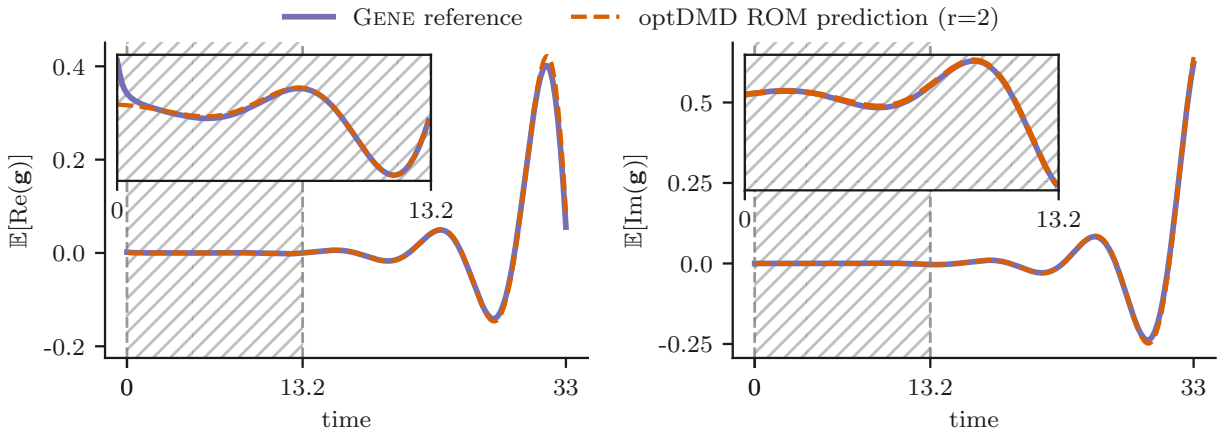


Figure 4: Cyclone Base Case benchmark scenario: The expected value of the real (left) and imaginary (right) components of the distribution function obtained using the $r = 2$ optDMD ROM versus the corresponding reference GENE data over the target time horizon. The training horizon $[0.0, 13.2]$ includes the transient phase.

predict the eigenvalue corresponding to the dominant ITG mode for both setups. For the first setup, the complex eigenvalue corresponding to the dominant mode computed with the ROM with reduced dimension $r = 1$ is $\tilde{\alpha}_{\text{ROM}} = 0.263 + 0.790i$. This is in excellent agreement with the reference GENE result, $\alpha_{\text{ref}} = 0.264 + 0.790i$, with relative errors of 0.364% for the growth rate and 0.004% for the frequency. Similarly, for the second setup where the optDMD ROM has reduced dimension $r = 2$, we obtain $\tilde{\alpha}_{\text{ROM}} = 0.265 + 0.788i$, with relative errors of 0.341% for the growth rate and 0.312% for the frequency.

Finally, we assess the computational efficiency of the ROMs. For the first setup (training during the saturated phase), constructing the ROM required 2.391 seconds on a single CPU core on Perlmutter. Evaluating this optDMD ROM over the target time horizon $[6.6, 32.993]$ took a total of 0.065 seconds, with 0.033 seconds spent over the training horizon and 0.032 seconds over the prediction horizon. Similarly, constructing the ROM for the second setup (training from $t_i = 0$) required 2.455 seconds. Its evaluation over the target time horizon $[0, 32.993]$ took 0.080 seconds, split between 0.033 seconds for training and 0.047 seconds for prediction. These results therefore demonstrate a significant reduction in runtime for both considered setups. Our optDMD ROMs decrease the evaluation time from 125.154 seconds (using four GPUs on a single GPU node on Perlmutter) to just 0.065 and 0.080 seconds (on a single CPU core on Perlmutter), respectively.

5.1.2. Reduced-order modeling predictions for variations in the normalized binormal wavenumber $k_y \rho_s$

We next investigate the ability of the ROM to make predictions across variations in one key input parameter, namely the normalized binormal wavenumber, $k_y \rho_s$. Here, we consider variations in $k_y \rho_s$ between 0.05 and 0.55, where the ITG instability is destabilized. Note that since the parametric dimension is only $d = 1$, we do not use (L)-Leja sparse grids for generating training data (sparse grids are defined for dimensions $d \geq 2$) nor (L)-Leja-based Lagrange interpolation for ROM predictions (cf. Remark 1).

Training a parametric reduced model using data for $n_p = 4$ parameter instances. We first consider a training dataset comprising only $n_p = 4$ instances of $k_y \rho_s$ including the extrema, namely $k_y \rho_s \in \{0.05, 0.20, 0.40, 0.55\}$. The snapshots for the training parameter instances are acquired over the micro-instability saturated phase. Details about the corresponding high-fidelity GENE runtimes and the time domain of interest $[t_i, t_f]$ for each of the four $k_y \rho_s$ values can be found in Table 1. As for the previous experiment, we save the respective distribution functions to disk every 100 time iterations. This amounts to a total of $n_t = 299$ snapshots per $k_y \rho_s$ instance, which means that the corresponding global snapshot matrix is of size $61,440 \times 4 \cdot 299 = 61,440 \times 1196$.

$k_y \rho_s$	GENE runtime (s)	$[t_i, t_f]$
0.05	454.647	[23.278, 53.062]
0.20	142.372	[7.569, 37.361]
0.40	145.320	[7.459, 48.335]
0.55	370.034	[18.551, 48.335]

Table 1: Cyclone Base Case benchmark scenario: setup for parametric reduced modeling using $n_p = 4$ training parameters.

Figure 5 plots the singular values on the left and the corresponding percentage of the retained energy on the right in solid orange line. The singular values decay fast: only $r = 2$ POD modes are sufficient to retain 99.99% of the energy. We therefore construct a parametric optDMD ROM with reduced dimension $r = 2$.

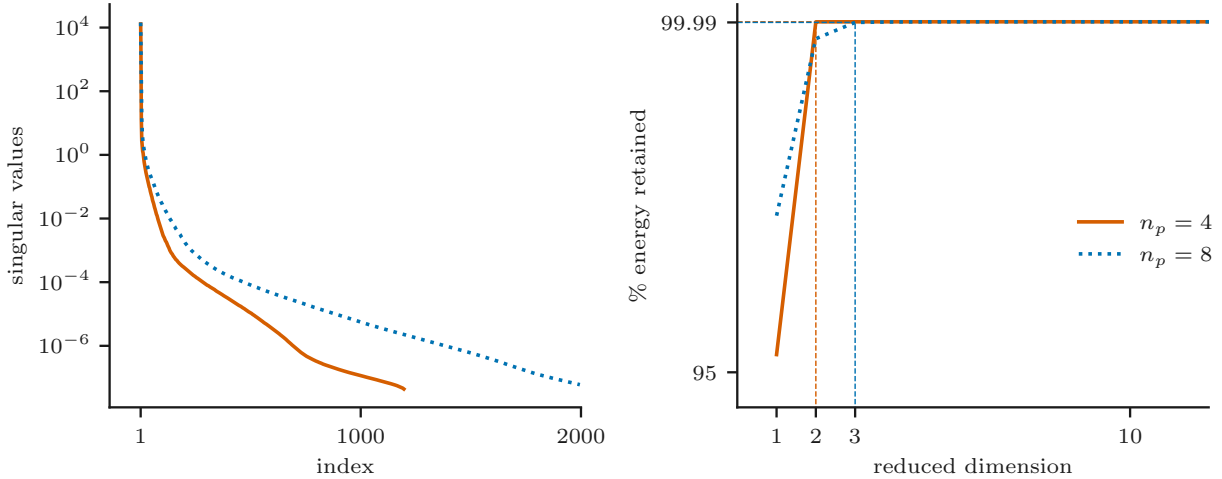


Figure 5: Cyclone Base Case benchmark scenario: Singular values (left) and corresponding retained energy (right) when constructing a parametric optDMD ROM using $n_p = 4$ parameter instances, namely $k_y \rho_s \in \{0.05, 0.20, 0.40, 0.55\}$ compared to using $n_p = 8$ instances, namely $k_y \rho_s \in \{0.05, 0.12, 0.20, 0.28, 0.38, 0.40, 0.48, 0.55\}$.

For evaluating the parametric ROM's ability to predict beyond its training data, we consider six testing parameter instances $k_y \rho_s \in \{0.10, 0.15, 0.25, 0.30, 0.45, 0.50\}$. Spline-based interpolation is used for computing the corresponding optDMD ROM predictions. Table 2 compares the eigenvalues corresponding to the dominant eigenmode obtained using our optDMD ROM ($\tilde{\alpha}_{\text{ROM}}$) against the reference eigenvalues computed by GENE (α_{ref}). The comparison is quantified by the relative error:

$$\text{err} [\%] = \frac{|\tilde{\alpha}_{\text{ROM}} - \alpha_{\text{ref}}|}{\alpha_{\text{ref}}} \times 100. \quad (8)$$

With the exception of $k_y \rho_s \in \{0.10, 0.15\}$, where the growth rate errors are 22.681% and 7.412%, all other errors remain below 3%, therefore demonstrating a reasonable prediction accuracy, considering that we used only $n_p = 4$ training parameter instances.

Increasing the number of training parameter instances to $n_p = 8$. We next investigate the effect of increasing the number of training parameter instances. Specifically, we double the number of instances to $n_p = 8$, using $k_y \rho_s = \{0.05, 0.12, 0.20, 0.28, 0.38, 0.40, 0.48, 0.55\}$. Details about the GENE high-fidelity simulations for the eight training parameter instances as well as the time domain of interest after the transient phases are found in Table 3. As before, we save the corresponding GENE distribution functions to disk every 100 time instants, which amounts to $n_t = 266$ snapshots per $k_y \rho_s$ instance. Therefore, the global snapshot matrix \mathbf{G} is of size $61,440 \times 8 \cdot 266 = 61,440 \times 2128$.

	α_{ref}	$\tilde{\alpha}_{\text{ROM}}$	Growth rate error (%)	Frequency error (%)
0.10	0.084 + 0.219i	0.103 + 0.222i	22.832	1.447
0.15	0.152 + 0.353i	0.163 + 0.356i	7.479	0.953
0.25	0.248 + 0.644i	0.241 + 0.640i	2.724	0.625
0.30	0.264 + 0.790i	0.256 + 0.784i	2.894	0.773
0.45	0.190 + 1.185i	0.191 + 1.191i	0.517	0.515
0.50	0.130 + 1.301i	0.128 + 1.310i	1.542	0.653

Table 2: Cyclone Base Case benchmark scenario: Comparison between the ROM prediction ($r = 2$, trained with $n_p = 4$ instances) and the GENE reference result for the eigenvalue corresponding to the ITG micro-instability mode, shown for six parameter instances beyond training.

$k_y \rho_s$	GENE runtime (s)	$[t_i, t_f]$
0.05	454.647	[23.278, 49.764]
0.12	202.679	[10.940, 37.431]
0.20	142.372	[7.569, 34.062]
0.28	124.049	[6.629, 33.123]
0.38	135.065	[7.109, 33.603]
0.40	145.320	[7.459, 33.952]
0.48	193.450	[10.070, 36.561]
0.55	370.034	[18.551, 45.036]

Table 3: Cyclone Base Case benchmark scenario: setup for parametric reduced modeling using $n_p = 8$ training parameters.

Figure 5 plots the singular values on the left and the percentage of retained energy on the right using dashed blue lines. The singular values exhibit a fast decay: only $r = 3$ POD modes are sufficient to retain 99.99% of the total energy. Consequently, we develop a parametric ROM with reduced dimension $r = 3$.

We begin by assessing the ROM’s capability to predict the growth rate and frequency of the dominant eigenmode. Table 4 presents a comparison between the ROM predictions and reference GENE results in terms of relative errors (8). Doubling the number of training parameters significantly improves the accuracy of the optDMD ROM predictions: the relative errors for $k_y \rho_s \in \{0.15, 0.20, 0.25, 0.30, 0.35, 0.45, 0.50\}$ fall below 1%, while the growth rate error for $k_y \rho_s = 0.10$ decreased from 22.681% to 2.454%.

	α_{ref}	$\tilde{\alpha}_{\text{ROM}}$	Growth rate error (%)	Frequency error (%)
0.10	0.084 + 0.219i	0.086 + 0.219i	2.454	0.190
0.15	0.152 + 0.353i	0.151 + 0.353i	0.618	0.082
0.25	0.248 + 0.644i	0.248 + 0.644i	0.017	0.033
0.30	0.264 + 0.790i	0.264 + 0.790i	0.158	0.030
0.45	0.190 + 1.185i	0.191 + 1.185i	0.295	0.014
0.50	0.130 + 1.301i	0.129 + 1.302i	0.860	0.040

Table 4: Cyclone Base Case benchmark scenario: Comparison between the ROM prediction ($r = 3$, trained with $n_p = 8$ instances) and the GENE reference result for the eigenvalue corresponding to the ITG micro-instability mode, shown for six parameter instances beyond training.

We next use the optDMD ROM for predicting the full distribution function for the six testing instances $k_y \rho_s \in \{0.10, 0.15, 0.25, 0.30, 0.45, 0.50\}$. This highlights a key advantage of ROMs over surrogate models that only predict high-fidelity linear operator eigenvalues (e.g., Refs. [31, 35, 58]): ROMs can predict the full distribution function, offering substantially more information. Table 5 presents the runtimes for the reference GENE simulations, performed using four GPUs on one Perlmutter GPU node over the full time horizons starting from $t = 0$, the time horizons of interest (corresponding to the micro-instability saturated phase) and the associated number of downsampled (by a factor of 100) snapshots, and the online ROM evaluation costs over the time horizon of interest. We first note the longer GENE runtimes for the extrema

of $k_y \rho_s$, which is due to needing more iterations to reach convergence. The offline cost for constructing the ROM with a reduced dimension $r = 3$ is 40.640 seconds. Online, evaluating the ROMs over the target time horizon costs at most 0.146 seconds, demonstrating a significant evaluation cost reduction.

$k_y \rho_s$	GENE runtime (s)	$[t_i, t_f]$	No. snapshots	ROM runtime (s)
0.10	245.007	[12.671, 42.458]	266	0.119
0.15	180.639	[9.200, 38.990]	266	0.118
0.25	133.659	[6.829, 34.122]	266	0.129
0.30	125.154	[6.600, 32.993]	266	0.129
0.45	161.607	[8.619, 38.410]	266	0.142
0.50	215.609	[10.980, 40.769]	266	0.146

Table 5: Cyclone Base Case benchmark scenario: Comparison between the reference GENE and ROM runtimes ($r = 3$, trained using $n_p = 8$ parameter instances) The ROM offline cost is 40.640 seconds.

To assess the ROM’s predictions of the distribution function, we compute two-dimensional averages as follows. To simplify the notation, let \mathbf{g} denote a distribution function (computed with a ROM or with GENE). First, \mathbf{g} is averaged over the time horizon of interest $[t_i, t_f]$ to obtain $\bar{\mathbf{g}}$ as:

$$\bar{\mathbf{g}}(k_x, z, v_{\parallel}, \mu) = \frac{1}{n_t} \sum_{t=t_i}^{t_f} \mathbf{g}(t, k_x, z, v_{\parallel}, \mu). \quad (9)$$

Afterwards, for each of the six possible two-dimensional combinations of directions, we compute 2D representations by averaging over the other two dimensions. For example, to obtain the projection onto the (k_x, z) plane, we average over v_{\parallel} and μ :

$$\langle \bar{\mathbf{g}} \rangle_{k_x, z}(k_x, z) = \frac{1}{n_{v_{\parallel}} n_{\mu}} \sum_{v_{\parallel}} \sum_{\mu} \bar{\mathbf{g}}(k_x, z, v_{\parallel}, \mu) \quad (10)$$

where $n_{v_{\parallel}}$ and n_{μ} denote the number of grid points along the averaged dimensions. This process is repeated for all six dimensional possible combinations.

For visualization purposes, we separate the real and imaginary parts of these 2D averages. Moreover, each of the resulting pairs of 2D slices are then normalized with respect to their respective maximum absolute value. This procedure scales each pair to the range $[-1, 1]$, facilitating a standardized visual comparison of the structure and magnitude of the data. The final normalized quantities for plotting, denoted by $\tilde{\mathbf{g}}$, are therefore given by:

$$\text{Re}[\tilde{\mathbf{g}}_{i,j}] = \frac{\text{Re}[\langle \bar{\mathbf{g}} \rangle_{i,j}]}{\max |\text{Re}[\langle \bar{\mathbf{g}} \rangle_{i,j}]|}, \quad \text{Im}[\tilde{\mathbf{g}}_{i,j}] = \frac{\text{Im}[\langle \bar{\mathbf{g}} \rangle_{i,j}]}{\max |\text{Im}[\langle \bar{\mathbf{g}} \rangle_{i,j}]|},$$

where $(i, j) \in \{k_x, z, v_{\parallel}, \mu\}^2$ and $i \neq j$.

Figures 6 and 7 present a comparison of all 2D slices of the time-averaged distribution function. Figure 6 plots the results for the testing parameter instance for which we obtained the largest growth rate and frequency errors, namely $k_y \rho_s = 0.10$. Conversely, Fig. 7 presents the results for $k_y \rho_s = 0.25$, for which we obtained the most accurate growth rate and frequency predictions. The 2D slices were generated using bicubic spline interpolation. Our ROM demonstrates a good agreement with the GENE slices across all combinations, effectively capturing the distribution function’s average features.

To summarize, this section demonstrated that low-dimensional optDMD ROMs can provide accurate predictions both beyond a training time horizon and for variations in the binomial wavenumber $k_y \rho_s$ for the CBC benchmark characterized by ITG-driven micro-instabilities. Next, we will assess the capabilities of parametric sparse grid optDMD ROMs in a real-world scenario involving variations in six plasma parameters.

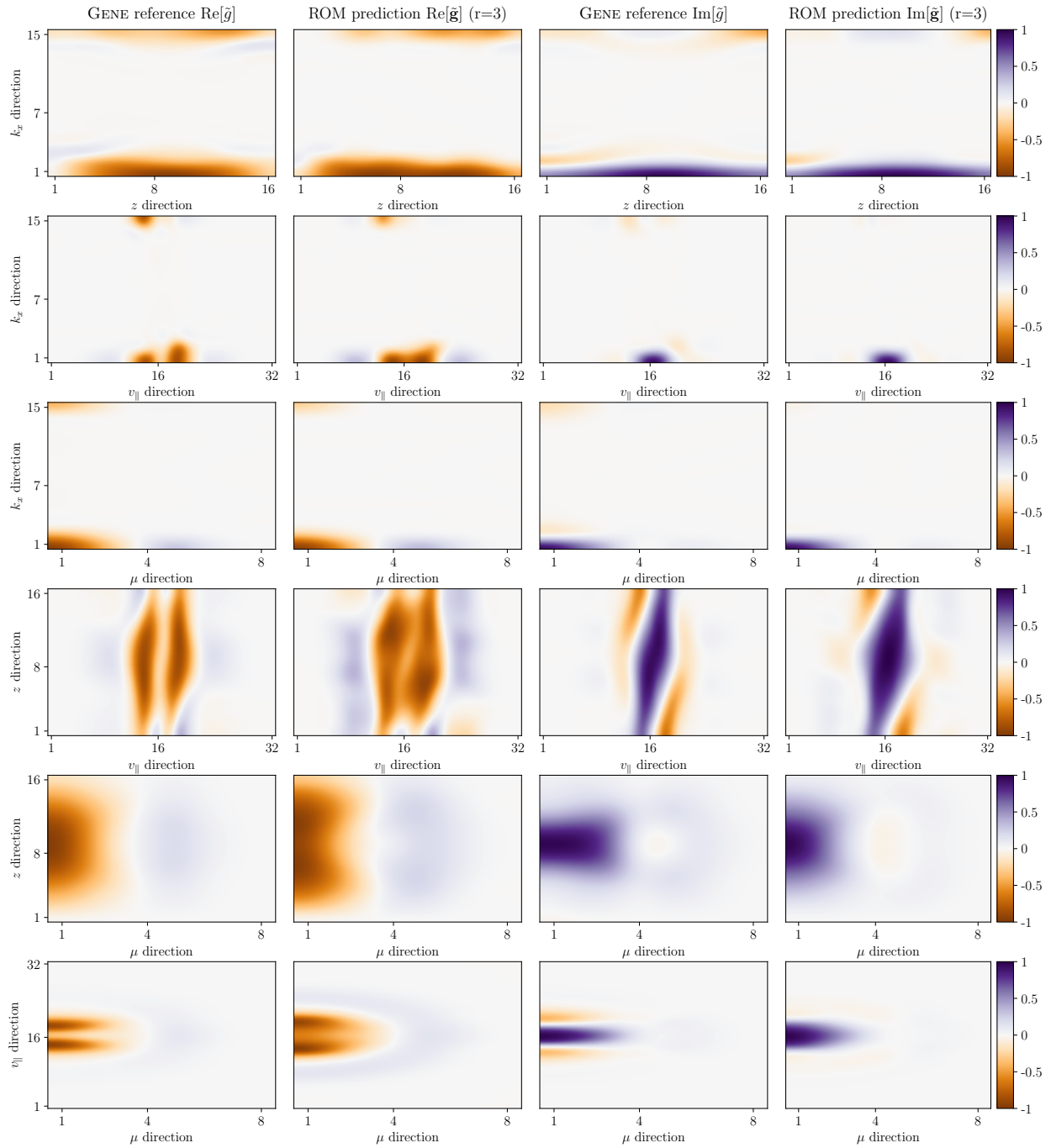


Figure 6: Cyclone Base Case benchmark scenario: Comparison between ROM prediction ($r = 3$ and $n_p = 8$ instances) and the GENE reference result for the full time-averaged gyrokinetic distribution function, shown for test case $k_y \rho_s = 0.10$.

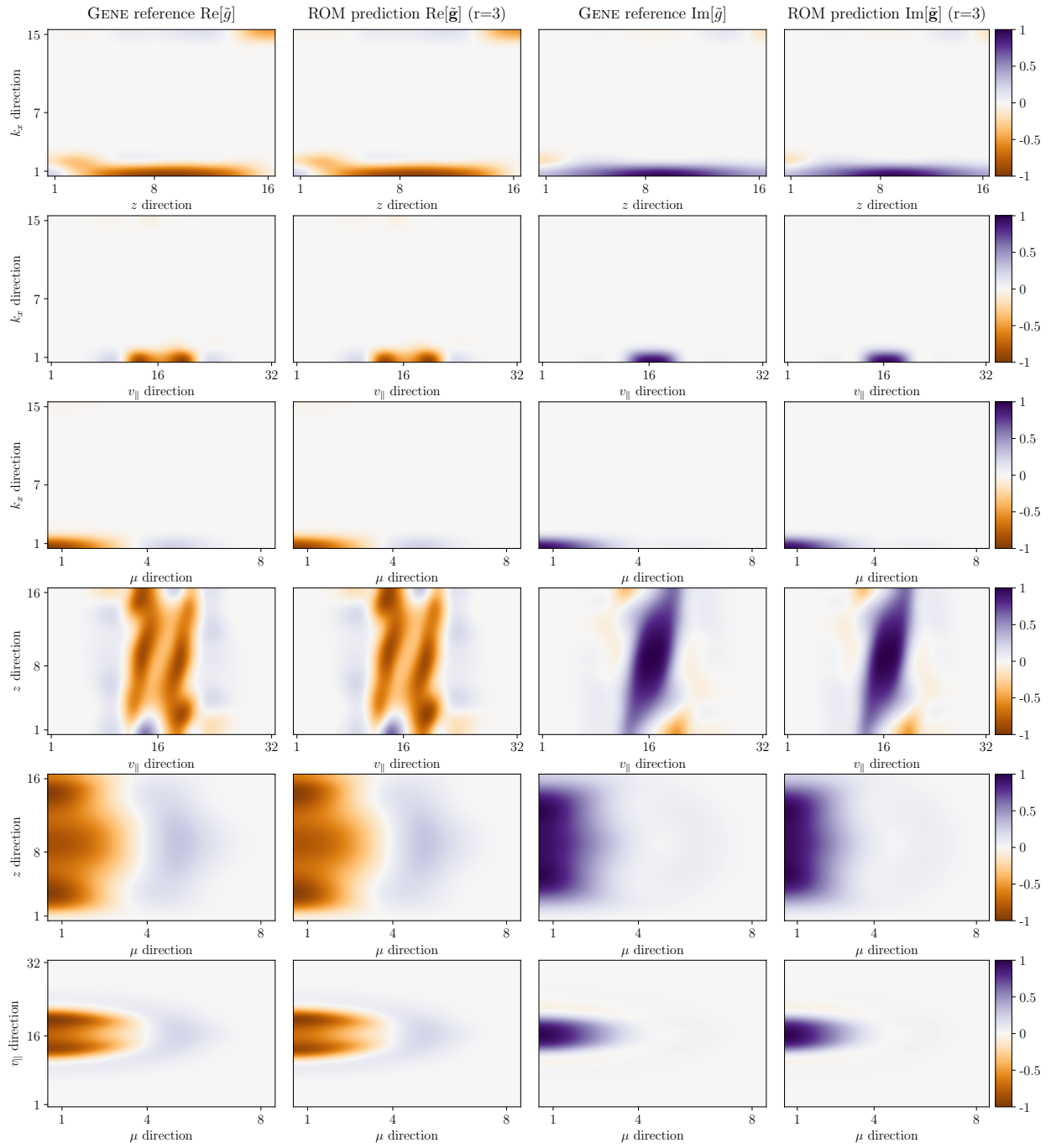


Figure 7: Cyclone Base Case benchmark scenario: Comparison between ROM prediction ($r = 3$ and $n_p = 8$ instances) and the GENE reference result for the full time-averaged gyrokinetic distribution function, shown for test case $k_y \rho_s = 0.25$.

5.2. Electron temperature gradient-driven micro-instability in the tokamak pedestal

The second scenario is a realistic problem focused on ETG mode simulation in the near-edge pedestal region of the DIII-D experiment, similar to the setup considered in Refs. [45, 86]. This is motivated by the study of electron-scale turbulent transport in the near-edge plasma of fusion experiments. Achieving the high core temperatures and densities required for self-heated (‘burning’) plasmas in future power plants necessitates the creation and sustainment of a steep gradient region at the plasma edge, known as the pedestal. The formation of this pedestal is a complex and still incompletely understood process, where plasma turbulence plays a crucial role. Driven by large spatial gradients in density and temperature, turbulence within the pedestal induces transport that contributes to its self-regulation. A significant driver of this turbulence is the ETG micro-instability [25, 54], which operates on sub-millimeter scales perpendicular to the magnetic field. Quantifying the impact of ETG turbulence on the pedestal structure is therefore essential for designing fusion configurations with enhanced energy confinement.

5.2.1. Setup for high-fidelity gyrokinetic simulations

We define the plasma behavior using six local parameters: $\{n_e, T_e, \omega_{n_e}, \omega_{T_e}, q, \tau\}$. Here, n_e is the electron density, and T_e is the electron temperature, $\omega_{n_e} = R/L_{n_e}$ and $\omega_{T_e} = R/L_{T_e}$ are the respective normalized (with respect to the major radius R) gradients, q is the safety factor, and $\tau = Z_{\text{eff}}T_e/T_i$, where Z_{eff} is the effective ion charge retained in the collision operator (here, a linearized Landau–Boltzmann operator) and T_i denotes the ion temperature. The ions are assumed to be adiabatic, and electromagnetic effects, computed consistently with the values of the electron temperature and density, are retained. Table 6 summarizes the setup for the six local input parameters. The first two parameters are varied by $\pm 10\%$ from their nominal values, while the remaining four inputs, including the two gradients, are varied by $\pm 20\%$. These variations were chosen to be consistent with typical experimental error bars.

input parameter	left bound	right bound
electron temperature T_e [keV]	0.357	0.436
electron density n_e [10^{19}m^{-3}]	4.042	4.941
temperature gradient $\omega_{T_e} = R/L_{T_e}$	148.800	223.200
density gradient $\omega_{n_e} = R/L_{n_e}$	70.400	105.600
electron-to-ion temperature ratio τ	1.152	1.728
safety factor q	3.628	5.443

Table 6: Electron temperature gradient-driven micro-instability scenario: Summary of the six input parameters and their respective bounds used to construct parametric reduced models.

The considered setup models DIII-D pedestal conditions, similar to those in Refs. [45, 86]. These conditions are characterized by large gradients that can generate substantial electron heat flux due to ETG turbulence. A comprehensive description of the experimental setup can be found in [45]. We note that a similar setup was also considered in Refs. [30, 33] where sparse grids were shown to enable efficient uncertainty propagation and sensitivity analysis, as well as the construction of a surrogate transport model for the ETG heat flux directly from nonlinear turbulence simulations.

We specify the magnetic geometry using a generalized Miller parametrization [19] using 64 Fourier harmonics to achieve a sufficiently accurate representation of the flux-surface at $\rho_{\text{tor}} = 0.95$, near the pedestal top. The high-fidelity linear GENE simulations employ $n = n_{k_x} \times n_{k_y} \times n_z \times n_{v_{\parallel}} \times n_{\mu} = 3 \times 1 \times 168 \times 32 \times 8 = 129,024$ degrees of freedom in the five-dimensional position–velocity space. Even with acceleration from four NVIDIA A100 GPUs, calculations of the linear growth rate typically require ~ 150 s wall clock time. The main cost arises from requiring a high resolution of points along the magnetic field line to accurately resolve the fast electron dynamics, which is endemic to electron scale instabilities in the pedestal [45].

5.2.2. Setup for sparse-grid-accelerated parametric data-driven reduced modeling

To learn a parametric optDMD ROM that embeds variations in the six considered plasma parameters, we generate training data using a level $L = 3$ sparse grid. This grid comprises $n_p = 28$ (L)-Leja points, computed

with respect to the uniform distribution with bounds given in Table 6. This approach is significantly more efficient than a full tensor grid: a mere three points per parameter in a tensor grid would necessitate $3^6 = 729$ GENE simulations, meaning our method requires a factor of 26 fewer simulations; cf. Fig. 1.

5.2.3. Reduced-order model predictions for parameters beyond training

We begin by selecting the time domains over the micro-instability saturation phase for training the parametric ROM. Since the 28 GENE simulations require a variable number of time steps to reach convergence, we ensure a consistent number of training snapshots by first discarding the initial 30% of the simulation history (which includes the respective transient phases) followed by truncating all simulations to the minimum number of remaining snapshots across all training instances. This resulted in 331 downsampled (by a factor of 10) snapshots per training parameter instance. The total number of snapshots is therefore $331 \times 28 = 9,268$, yielding a global snapshot matrix $\mathbf{G} \in \mathbb{C}^{129,024 \times 9,268}$. This setup is summarized in Table 7. This table also includes the minimum, maximum, and average GENE runtime, with the average runtime being 91.695 seconds. The parametric ROM offline cost was 374.889 seconds on one Perlmutter CPU node.

Setup for acquiring training data	Minimum	Maximum	Average
Computed time steps (GENE)	4,729	11,169	8,174.36
GENE runtime (s)	52.583	126.431	91.695
t_i	0.027	0.056	0.043
t_f	0.091	0.112	0.101

Table 7: Electron temperature gradient-driven micro-instability scenario: Details about the GENE simulations used to acquire the training data.

We then determine the reduced dimension for the parametric ROM. Figure 8 plots the singular values and corresponding retained energy, demonstrating that $r = 4$ POD modes retain over 99.99% of the total energy. We therefore construct a sparse grid parametric optDMD ROM with a reduced dimension of $r = 4$.

Next, we assess the prediction capabilities of this ROM using 20 testing parameter values. These values are pseudo-randomly generated from a uniform distribution with bounds given in Table 6. The average GENE runtime for these testing runs on four GPUs on one GPU node on Perlmutter was 83.960 seconds, with the minimum runtime being 54.245 seconds and the maximum 161.686 seconds.

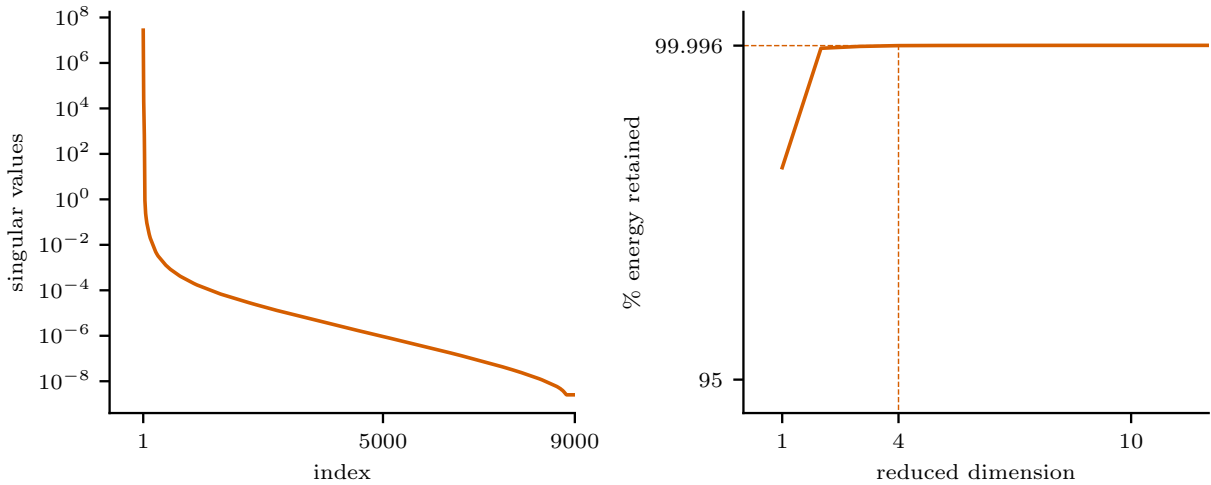


Figure 8: Electron temperature gradient-driven micro-instability scenario: Singular values (left) and corresponding retained energy (right). The training data consists of the GENE distribution function over the respective micro-instability saturation phase for $n_p = 28$ sparse (L)-Leja grid parameter instances.

Table 8 compares the dominant eigenvalue from GENE with our ROM’s predictions for all 20 testing parameter values in terms of their relative errors (8). Most predicted growth rates and frequencies exhibit errors $< 1\%$; exceptions include test cases 9 (8.715% growth rate error) and 18 (5.229% growth rate error). These results underscore the effectiveness of sparse grid interpolation in parametric ROMs.

Test Case	α_{ref}	$\tilde{\alpha}_{\text{ROM}}$	Growth Rate Error (%)	Frequency Error (%)
1	102.218 – 425.998i	100.551 – 425.623i	1.630	0.088
2	143.815 – 184.055i	144.198 – 186.111i	0.266	1.117
3	151.346 – 227.680i	152.400 – 228.618i	0.696	0.412
4	123.600 – 422.313i	125.897 – 421.017i	1.858	0.307
5	181.105 – 401.320i	179.419 – 401.157i	0.931	0.041
6	179.880 – 322.169i	180.497 – 322.710i	0.343	0.168
7	180.735 – 326.660i	181.072 – 327.666i	0.187	0.308
8	167.890 – 339.058i	168.548 – 338.864i	0.392	0.057
9	67.166 – 598.561i	73.020 – 595.118i	8.715	0.575
10	112.340 – 522.321i	114.453 – 522.102i	1.881	0.042
11	147.970 – 227.259i	145.208 – 227.864i	1.867	0.266
12	163.487 – 224.390i	161.522 – 226.409i	1.202	0.900
13	145.603 – 259.407i	144.531 – 259.162i	0.736	0.095
14	129.197 – 289.963i	129.206 – 289.191i	0.007	0.266
15	180.474 – 300.428i	180.149 – 302.816i	0.180	0.795
16	129.533 – 412.653i	130.137 – 412.337i	0.467	0.076
17	145.947 – 207.040i	145.848 – 208.140i	0.068	0.531
18	103.983 – 590.134i	98.473 – 587.675i	5.299	0.417
19	143.528 – 389.056i	145.644 – 389.009i	1.474	0.012
20	146.416 – 317.500i	146.171 – 317.413i	0.167	0.027

Table 8: Electron temperature gradient-driven micro-instability scenario: Comparison between the ROM prediction ($r = 4$, trained with $n_p = 28$ instances) and the GENE reference result for the eigenvalue corresponding to the ETG micro-instability mode, shown for 20 parameter instances beyond training.

We provide a more detailed assessment of the ROM’s prediction capabilities, focusing on testing parameters 20 and 9 from Table 8, which correspond to the smallest and largest eigenvalue prediction errors, respectively. We use the optDMD ROM to predict the full distribution functions over the respective time horizons of interest. Figures 9 and 10 plot all 2D time-averaged slices of the distribution function for cases 9 and 20, computed as described in Sec. 5.1.2. For both cases, good agreement is observed between the ROM predictions and the GENE reference results, demonstrating that the ROM accurately captures the averaged features of the distribution function.

In addition, we also utilize the predicted distribution functions to derive relevant physical quantities of interest. Specifically, we compute moments of the distribution function, namely the electrostatic potential ϕ , the parallel component of the vector potential A_{\parallel} , and the parallel component of the effective magnetic field B_{\parallel}^* along the magnetic field direction z , as summarized in Sec. 3.1. Given the relevance of these quantities, we also investigate the impact of the ROM reduced dimension. To this aim, we consider parametric sparse grid optDMD ROMs with reduced dimensions $r = 1$ and $r = 4$. Figures 11 and 12 plot ϕ , A_{\parallel} , and B_{\parallel}^* predicted by the parametric ROM (blue dashed line) compared to the reference GENE results (orange solid line) for testing parameters 9 and 20, respectively. For a consistent visualization, the results were normalized such that the inner product of the fields is unity, that is, $\langle \phi, \phi \rangle = 1$. In both cases, the ROM with reduced dimension $r = 1$ fails to capture the electromagnetic fields, whereas the ROM with reduced dimension $r = 4$ produces much more accurate predictions. This shows that even though a large amount of energy is contained in a the first POD mode, a larger number of modes is necessary to construct accurate parametric ROMs.

Finally, for the computed parametric ROM with reduced dimension $r = 4$, we investigate the $r - 1$ stable eigenmodes predicted by the ROM. In general, practitioners are interested in these stable modes for their

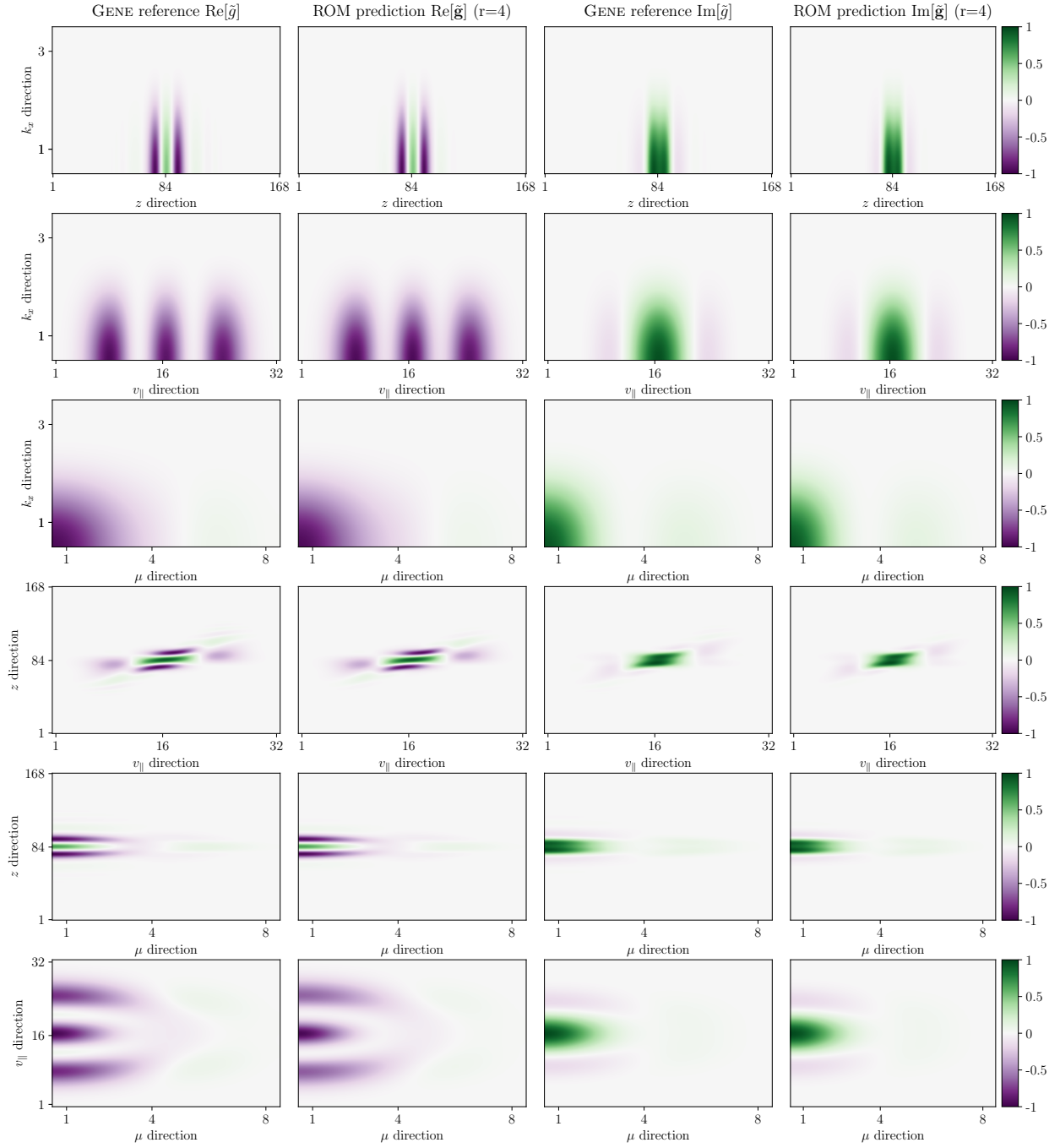


Figure 9: Electron temperature gradient-driven micro-instability scenario: Comparison between ROM prediction ($r = 4$) and the GENE reference result for the full time-averaged gyrokinetic distribution function, shown for test case 20.

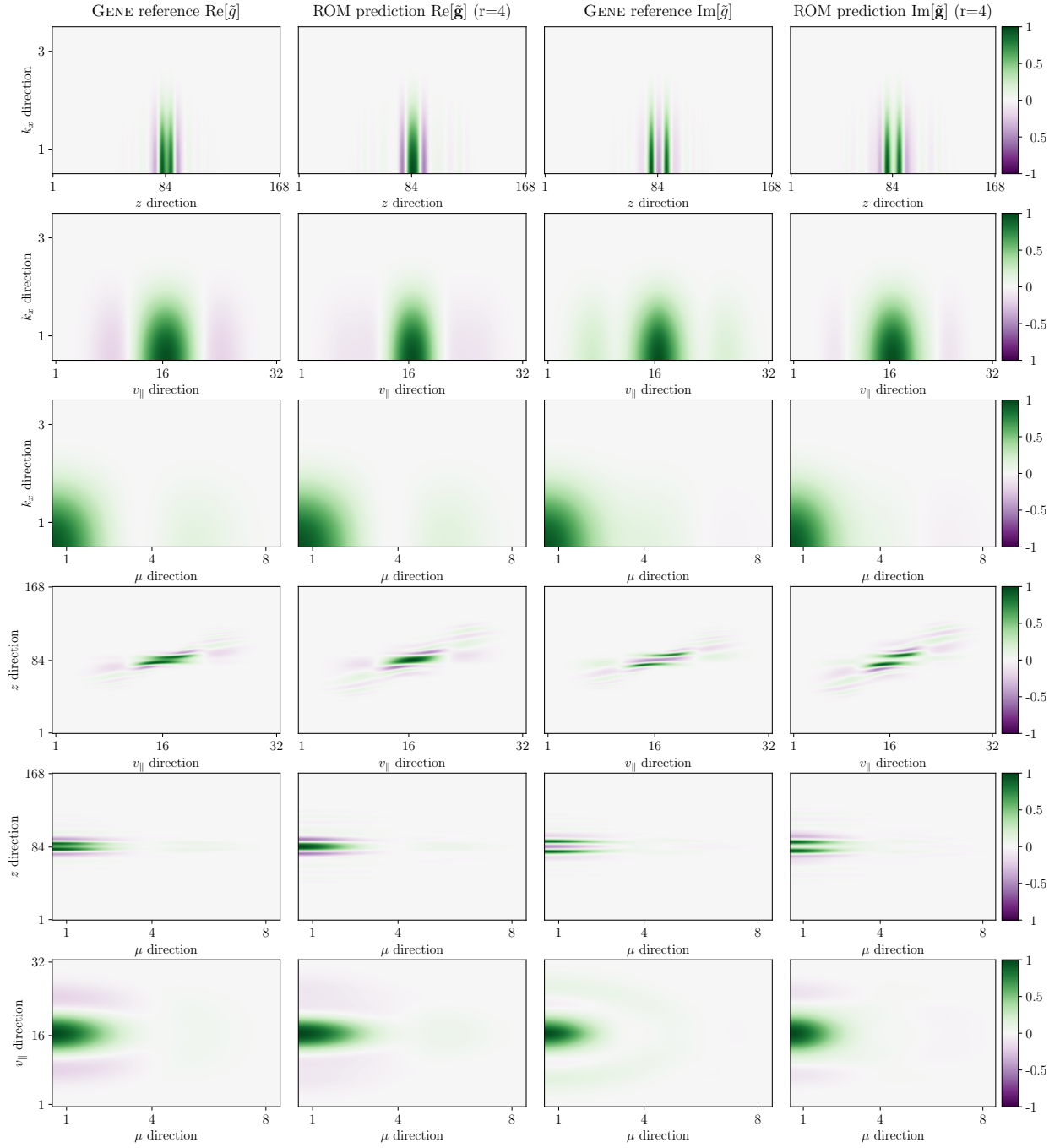


Figure 10: Electron temperature gradient-driven micro-instability scenario: Comparison between ROM prediction ($r = 4$) and the GENE reference result for the full time-averaged gyrokinetic distribution function, shown for test case 9.

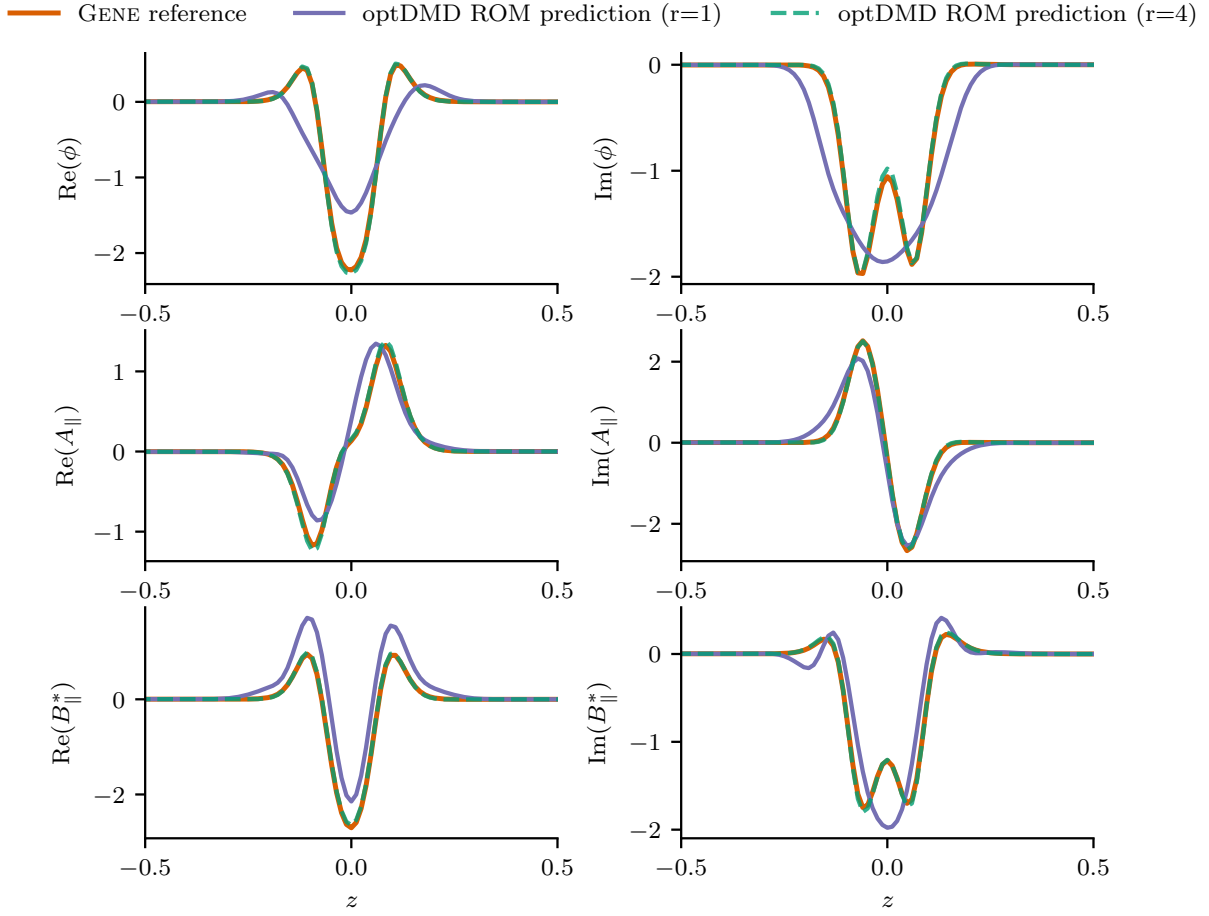


Figure 11: Electron temperature gradient-driven micro-instability scenario: Comparison between the ROM prediction ($r = 1$ and $r = 4$) and the GENE reference result for the electromagnetic fields (derived from the distribution function) for test case 20. Increasing the reduced dimension r improves the ROM prediction accuracy.

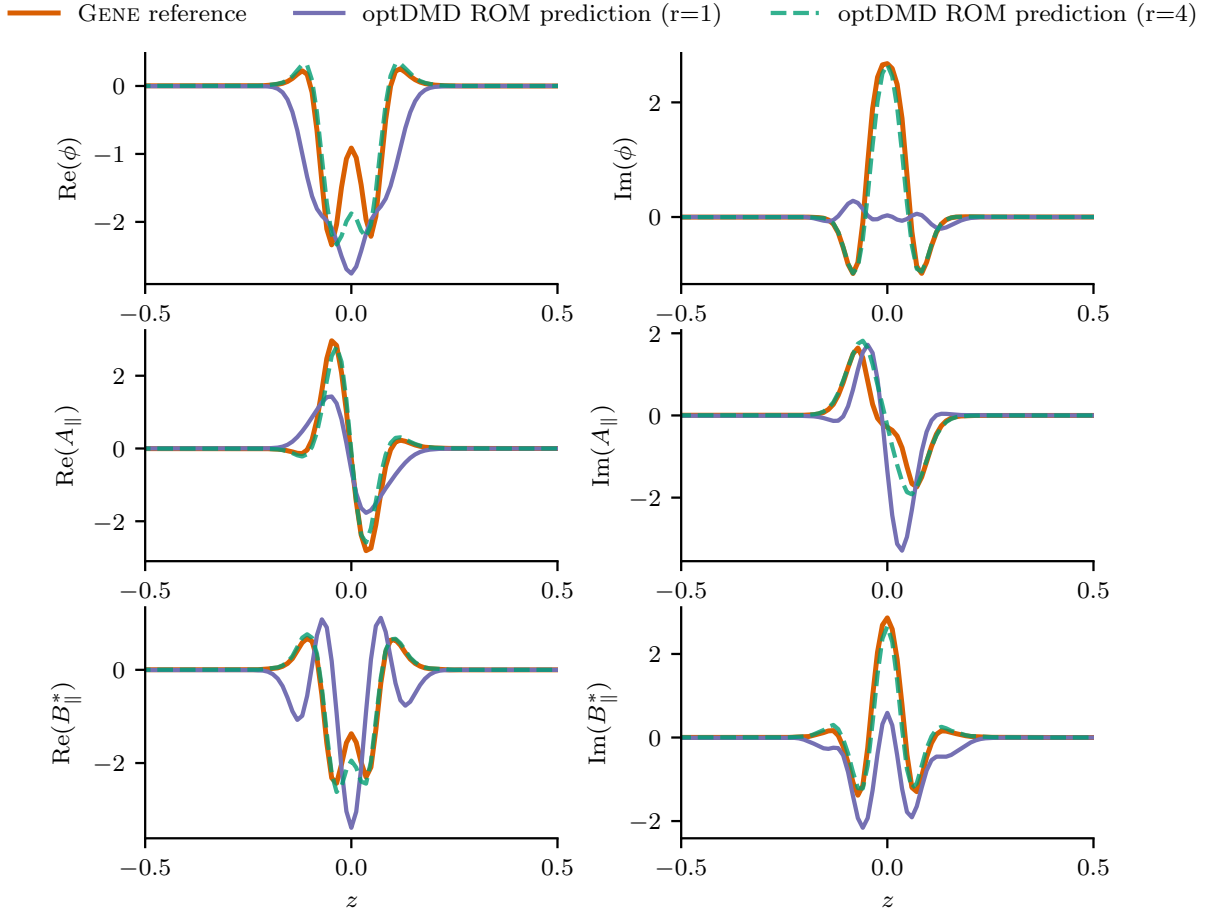


Figure 12: Electron temperature gradient-driven micro-instability scenario: Comparison between the ROM prediction ($r = 1$ and $r = 4$) and the GENE reference result for the electromagnetic fields (derived from the distribution function) for test case 9. Increasing the reduced dimension r improves the ROM prediction accuracy.

ability to affect saturation and transport via nonlinear coupling mechanisms [83]. Therefore, being able to accurately predict not only the dominant instability but also the subdominant and stable eigenmodes is a desirable property of parametric ROMs. Figures 13 and 14 plot the the four eigenvalues predicted by the parametric ROM compared with the ~ 200 eigenvalues as computed by the GENE linear eigenvalue solver (details discussed in Sec. 4.1), for testing parameters 20 and 9. For both cases, it is clear to see that the growth rate and frequency of the most unstable mode is recovered with high accuracy. Since the GENE linear eigenvalue solver produces many more stable modes than the reduced dimension of our ROM, however, comparing stable modes between the two is slightly more involved. Therefore, we target specific regions of the stable mode spectrum using the shift-and-invert preconditioning and compare with the $r - 1$ stable eigenmodes from our ROM. Impressively, the first stable mode predicted by our optDMD ROM is $\tilde{\alpha}_{\text{ROM}} = -35.416 + 32.173i$, compared to the first stable mode computed by the eigenvalue solver is $\alpha_{\text{ref}} = -33.262 + 29.852i$, resulting in a 6.476% and 7.775% relative error in growth rate and frequency, respectively. Although a direct identification of all stable modes may be hard to conclude, visual inspection suggests that there are many possible candidate modes that may correspond to the stable modes recovered by the ROM. Furthermore, in contrast to cases studied elsewhere [27, 47, 73, 88], for the ETG case currently considered, these subdominant and stable modes evidently contribute with very little energy to the overall spectrum; therefore, we leave further exploration of stable and subdominant modes for future work, while noting that the proposed approach remains promising.

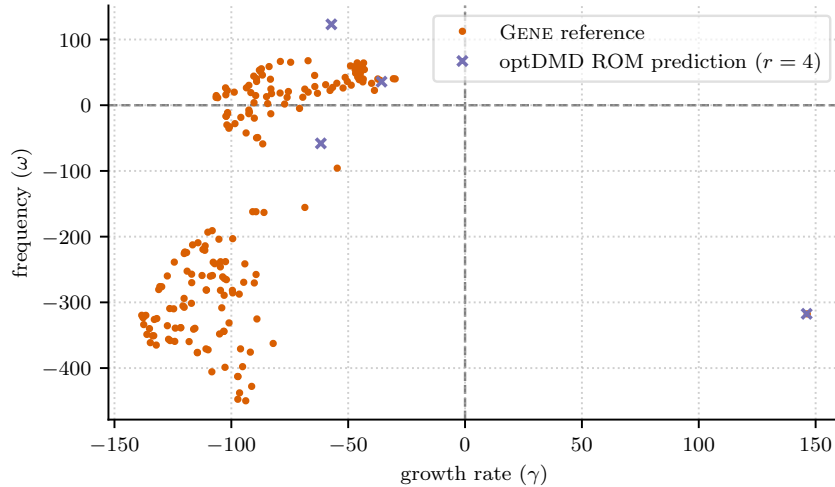


Figure 13: Electron temperature gradient-driven micro-instability scenario: Comparison between the ROM prediction ($r = 4$) and the GENE reference result for the eigenvalue spectrum for test case 20.

6. Conclusion

Parametric data-driven reduced-order modeling play an essential role in enabling tasks like design optimization, control, uncertainty quantification, sensitivity analysis, and inverse problems, especially in the context of applications with large-scale numerical models. A key challenge, however, is to ensure that the training cost of these reduced models is not exceedingly high. One effective strategy is to employ efficient techniques for selecting the training parameter instances. This paper investigated the use of sparse grids constructed using (L)-Leja points for efficiently training parametric reduced models. Since this point sequence is nested and grows slowly with the sparse grid level, the cardinality of the resulting sparse grid remains reasonably low in higher-dimensional settings. Moreover, (L)-Leja points are also excellent for interpolation, which can also be exploited in the context of parametric reduced modeling for computing predictions for arbitrary input parameter values within the interpolation domain. We have demonstrated the effectiveness

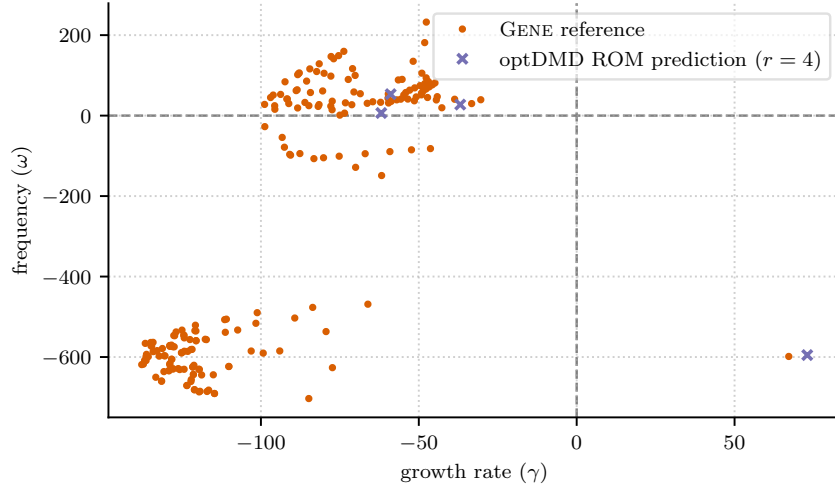


Figure 14: Electron temperature gradient-driven micro-instability scenario: Comparison between the ROM prediction ($r = 4$) and the GENE reference result for the eigenvalue spectrum for test case 9.

of this approach in the context of plasma micro-instability simulations in fusion experiments. In a real-world scenario with six parameter instances focused on electron temperature gradient driven modes at the edge of fusion experiments, a mere 28 parameter instances were sufficient to construct an accurate parametric reduced model based on optimized dynamic mode decomposition. We note that the ideas presented in this paper are generic, extending beyond plasma micro-instability simulations and linear parametric reduced models. A potential limitation for applications with computationally expensive models is that the sparse (L)-Leja grid might contain a large number of points if the input parameter space is high-dimensional. One way to address this is to incorporate adaptivity into the sparse grid procedure, which was shown to be effective for uncertainty propagation [30, 31] and surrogate model construction [33].

Acknowledgement

This research used resources of the National Energy Research Scientific Computing Center (NERSC), a U.S. Department of Energy Office of Science User Facility located at Lawrence Berkeley National Laboratory, operated under Contract No. DE-AC02-05CH11231 using NERSC award FES-ERCAP0026282. I.-G. F. was supported in part by NSF Grant DMS-2436357 “MATH-DT: Advancing Digital Twins for Jet Engines Through Mathematical and Computational Innovation.” B. J. F. was supported in part by U.S. Department of Energy Grant No. DE-FG02-93ER54222.

References

- [1] Amsallem, D., Farhat, C., 2011. An Online Method for Interpolating Linear Parametric Reduced-Order Models. *SIAM Journal on Scientific Computing* 33, 2169–2198. doi:10.1137/100813051.
- [2] Andreuzzi, F., Demo, N., Rozza, G., 2023. A Dynamic Mode Decomposition Extension for the Forecasting of Parametric Dynamical Systems. *SIAM Journal on Applied Dynamical Systems* 22, 2432–2458. doi:10.1137/22M1481658.
- [3] Artigues, V., Greif, R., Jenko, F., 2025. Accelerating Hasegawa–Wakatani simulations with machine learning for out-of-distribution predictions 67, 045018. doi:10.1088/1361-6587/adbb1c.
- [4] Askham, T., Kutz, J.N., 2018. Variable projection methods for an optimized dynamic mode decomposition. *SIAM Journal on Applied Dynamical Systems* 17, 380–416. doi:10.1137/M1124176.

- [5] Atchley, S., Zimmer, C., Lange, J., Bernholdt, D., Melesse Vergara, V., Beck, T., Brim, M., Budiardja, R., Chandrasekaran, S., Eisenbach, M., Evans, T., Ezell, M., Frontiere, N., Georgiadou, A., Glenski, J., Grete, P., Hamilton, S., Holmen, J., Huebl, A., Jacobson, D., Joubert, W., McMahon, K., Merzari, E., Moore, S., Myers, A., Nichols, S., Oral, S., Papatheodore, T., Perez, D., Rogers, D.M., Schneider, E., Vay, J.L., Yeung, P.K., 2023. Frontier: Exploring Exascale, in: Proceedings of the International Conference for High Performance Computing, Networking, Storage and Analysis, Association for Computing Machinery, New York, NY, USA. pp. 1–16. doi:10.1145/3581784.3607089.
- [6] Barnes, M., Dickinson, D., Dorland, W., Hill, P.A., Parker, J.T., Roach, C.M., Giacomini, M., Mandell, N., Numata, R., Schuett, T., Biggs-Fox, S., Christen, N., Parisi, J., Wilkie, G., Anton, L., Ball, J., Baumgaertel, J., Colyer, G., Hardman, M., Hein, J., Highcock, E., Howes, G., Jackson, A., Kotschenreuther, M.T., Lee, J., Leggate, H., Mauriya, A., Patel, B., Tatsuno, T., Van Wyk, F., 2024. Gs2 v8.2.1. doi:10.5281/zenodo.14022029.
- [7] Beer, M.A., Cowley, S.C., Hammett, G.W., 1995. Field-aligned coordinates for nonlinear simulations of tokamak turbulence. *Physics of Plasmas* 2, 2687–2700. doi:10.1063/1.871232.
- [8] Belli, E.A., Candy, J., Sfiligoi, I., 2022. Spectral Transition of Multiscale Turbulence in the Tokamak Pedestal. *Plasma Physics and Controlled Fusion* 65, 024001. doi:10.1088/1361-6587/aca9fa.
- [9] Benner, P., Gugercin, S., Willcox, K., 2015. A Survey of Projection-Based Model Reduction Methods for Parametric Dynamical Systems. *SIAM Review* 57, 483–531. doi:10.1137/130932715.
- [10] Berrut, J.P., Trefethen, L.N., 2004. Barycentric Lagrange Interpolation. *SIAM Review* 46, 501–517. doi:10.1137/S0036144502417715.
- [11] Beurskens, M., Bozhnikov, S., Ford, O., Xanthopoulos, P., Zocco, A., Turkin, Y., Alonso, A., Beidler, C., Calvo, I., Carralero, D., Estrada, T., Fuchert, G., Grulke, O., Hirsch, M., Ida, K., Jakubowski, M., Killer, C., Krychowiak, M., Kwak, S., Lazerson, S., Langenberg, A., Lunsford, R., Pablant, N., Pasch, E., Pavone, A., Reimold, F., Romba, T., von Stechow, A., Smith, H., Windisch, T., Yoshinuma, M., Zhang, D., Wolf, R., W7-X Team, t., 2021. Ion temperature clamping in Wendelstein 7-X electron cyclotron heated plasmas. *Nuclear Fusion* 61, 116072. doi:10.1088/1741-4326/ac1653.
- [12] Binev, P., Cohen, A., Dahmen, W., DeVore, R., Petrova, G., Wojtaszczyk, P., 2011. Convergence Rates for Greedy Algorithms in Reduced Basis Methods. *SIAM Journal on Mathematical Analysis* 43, 1457–1472. doi:10.1137/100795772.
- [13] Bird, R., Tan, N., Luedtke, S.V., Harrell, S.L., Taufer, M., Albright, B., 2021. VPIC 2.0: Next generation particle-in-cell simulations. *IEEE Transactions on Parallel and Distributed Systems* 33, 952–963.
- [14] Brizard, A.J., Hahm, T.S., 2007. Foundations of nonlinear gyrokinetic theory. *Reviews of Modern Physics* 79, 421–468. doi:10.1103/RevModPhys.79.421.
- [15] Buchfink, P., Glas, S., Haasdonk, B., Unger, B., 2024. Model reduction on manifolds: A differential geometric framework. *Physica D: Nonlinear Phenomena* 468, 134299. doi:https://doi.org/10.1016/j.physd.2024.134299.
- [16] Bui-Thanh, T., Willcox, K., Ghattas, O., 2008a. Model Reduction for Large-Scale Systems with High-Dimensional Parametric Input Space. *SIAM Journal on Scientific Computing* 30, 3270–3288. doi:10.1137/070694855.
- [17] Bui-Thanh, T., Willcox, K., Ghattas, O., 2008b. Parametric Reduced-Order Models for Probabilistic Analysis of Unsteady Aerodynamic Applications. *AIAA Journal* 46, 2520–2529. doi:10.2514/1.35850.
- [18] Bungartz, H.J., Griebel, M., 2004. Sparse grids. *Acta Numerica* 13, 147–269. doi:10.1017/S0962492904000182.
- [19] Candy, J., 2009. A unified method for operator evaluation in local Grad-Shafranov plasma equilibria. *Plasma Physics and Controlled Fusion* 51, 105009. doi:10.1088/0741-3335/51/10/105009.
- [20] Chen, K.K., Tu, J.H., Rowley, C.W., 2012. Variants of dynamic mode decomposition: boundary condition, Koopman, and Fourier analyses. *Journal of nonlinear science* 22, 887–915. doi:https://doi.org/10.1007/s00332-012-9130-9.

- [21] Chen, Y., Parker, S.E., 2007. Electromagnetic gyrokinetic δf particle-in-cell turbulence simulation with realistic equilibrium profiles and geometry. *Journal of Computational Physics* 220, 839–855. doi:<https://doi.org/10.1016/j.jcp.2006.05.028>.
- [22] Cheung, S.W., Choi, Y., Springer, H.K., Kadeethum, T., 2024. Data-scarce surrogate modeling of shock-induced pore collapse process. *Shock Waves* 34, 237–256. doi:10.1007/s00193-024-01177-2.
- [23] Crandall, P., Jarema, D., Doerk, H., Pan, Q., Merlo, G., Görler, T., Navarro, A.B., Told, D., Maurer, M., Jenko, F., 2020. Multi-species collisions for delta-f gyrokinetic simulations: Implementation and verification with GENE. *Computer Physics Communications* 255, 107360. doi:<https://doi.org/10.1016/j.cpc.2020.107360>.
- [24] Dimits, A.M., Bateman, G., Beer, M.A., Cohen, B.I., Dorland, W., Hammett, G.W., Kim, C., Kinsey, J.E., Kotschenreuther, M., Kritz, A.H., Lao, L.L., Mandrekas, J., Nevins, W.M., Parker, S.E., Redd, A.J., Shumaker, D.E., Sydora, R., Weiland, J., 2000. Comparisons and physics basis of tokamak transport models and turbulence simulations. *Physics of Plasmas* 7, 969–983. doi:10.1063/1.873896.
- [25] Dorland, W., Jenko, F., Kotschenreuther, M., Rogers, B.N., 2000. Electron Temperature Gradient Turbulence. *Physical Review Letters* 85, 5579–5582. doi:10.1103/PhysRevLett.85.5579.
- [26] Dudkovskaia, A.V., Li, D., Candy, J., Belli, E.A., Yang, C., 2025. Dynamic mode decomposition for gyrokinetic eigenmode analysis. *Plasma Physics and Controlled Fusion* 67, 065033. doi:10.1088/1361-6587/addb73.
- [27] Faber, B.J., Pueschel, M.J., Terry, P.W., Hegna, C.C., Roman, J.E., 2018. Stellarator microinstabilities and turbulence at low magnetic shear. *Journal of Plasma Physics* 84, 905840503. doi:10.1017/S0022377818001022.
- [28] Faraji, F., Reza, M., Knoll, A., Kutz, J.N., 2023a. Dynamic mode decomposition for data-driven analysis and reduced-order modeling of $E \times B$ plasmas: I. Extraction of spatiotemporally coherent patterns. *Journal of Physics D: Applied Physics* 57, 065201. doi:10.1088/1361-6463/ad0910.
- [29] Faraji, F., Reza, M., Knoll, A., Kutz, J.N., 2023b. Dynamic mode decomposition for data-driven analysis and reduced-order modeling of $E \times B$ plasmas: II. Dynamics forecasting. *Journal of Physics D: Applied Physics* 57, 065202. doi:10.1088/1361-6463/ad0911.
- [30] Farçaş, I.G., Merlo, G., Jenko, F., 2022. A general framework for quantifying uncertainty at scale. *Communications Engineering* 1, 43. doi:10.1038/s44172-022-00045-0.
- [31] Farçaş, I.G., Siena, A.D., Jenko, F., 2021. Turbulence suppression by energetic particles: a sensitivity-driven dimension-adaptive sparse grid framework for discharge optimization. *Nuclear Fusion* 61, 056004. doi:10.1088/1741-4326/abcc8.
- [32] Farçaş, I.G., Görler, T., Bungartz, H.J., Jenko, F., Neckel, T., 2020. Sensitivity-driven adaptive sparse stochastic approximations in plasma microinstability analysis. *Journal of Computational Physics* 410, 109394. doi:<https://doi.org/10.1016/j.jcp.2020.109394>.
- [33] Farçaş, I.G., Merlo, G., Jenko, F., 2024. Advanced surrogate model for electron-scale turbulence in tokamak pedestals. *Journal of Plasma Physics* 90, 905900510. doi:10.1017/S0022377824001314.
- [34] Feng, L., Benner, P., 2021. On error estimation for reduced-order modeling of linear non-parametric and parametric systems. *ESAIM: Mathematical Modelling and Numerical Analysis* 55, 561–594. doi:10.1051/m2an/2021001.
- [35] Fransson, E., Gillgren, A., Ho, A., Borsander, J., Lindberg, O., Rieck, W., Åqvist, M., Strand, P., 2023. A fast neural network surrogate model for the eigenvalues of QuaLiKiz. *Physics of Plasmas* 30, 123904. doi:10.1063/5.0174643.
- [36] Fu, J., Xiao, D., Fu, R., Li, C., Zhu, C., Arcucci, R., Navon, I.M., 2023. Physics-data combined machine learning for parametric reduced-order modelling of nonlinear dynamical systems in small-data regimes. *Computer Methods in Applied Mechanics and Engineering* 404, 115771. doi:<https://doi.org/10.1016/j.cma.2022.115771>.

- [37] Galletti, G., Paischer, F., Setinek, P., Hornsby, W., Zanisi, L., Carey, N., Pamela, S., Brandstetter, J., 2025. 5D Neural Surrogates for Nonlinear Gyrokinetic Simulations of Plasma Turbulence. URL: <https://arxiv.org/abs/2502.07469>, arXiv:2502.07469.
- [38] Garbet, X., Idomura, Y., Villard, L., Watanabe, T., 2010. Gyrokinetic simulations of turbulent transport. *Nuclear Fusion* 50, 043002. doi:10.1088/0029-5515/50/4/043002.
- [39] Germaschewski, K., Allen, B., Dannert, T., Hrywniak, M., Donaghy, J., Merlo, G., Ethier, S., D’Azevedo, E., Jenko, F., Bhattacharjee, A., 2021. Toward Exascale Whole-Device Modeling of Fusion Devices: Porting the GENE Gyrokinetic Microturbulence Code to GPU. *Physics of Plasmas* 28, 062501. doi:10.1063/5.0046327.
- [40] Gerstner, T., Griebel, M., 2003. Dimension-Adaptive Tensor-Product Quadrature. *Computing* 71, 65–87. doi:10.1007/s00607-003-0015-5.
- [41] Gopakumar, V., Pamela, S., Zanisi, L., Li, Z., Gray, A., Brennand, D., Bhatia, N., Stathopoulos, G., Kusner, M., Peter Deisenroth, M., Anandkumar, A., the JOREK Team, Team, M., 2024. Plasma surrogate modelling using Fourier neural operators. *Nuclear Fusion* 64, 056025. doi:10.1088/1741-4326/ad313a.
- [42] Grepl, M.A., Maday, Y., Nguyen, N.C., Patera, A.T., 2007. Efficient reduced-basis treatment of non-affine and nonlinear partial differential equations. *ESAIM: Mathematical Modelling and Numerical Analysis* 41, 575–605. doi:10.1051/m2an:2007031.
- [43] Görler, T., Lapillonne, X., Brunner, S., Dannert, T., Jenko, F., Merz, F., Told, D., 2011. The global version of the gyrokinetic turbulence code GENE. *Journal of Computational Physics* 230, 7053–7071. doi:<https://doi.org/10.1016/j.jcp.2011.05.034>.
- [44] Hakim, A.H., Mandell, N.R., Bernard, T.N., Francisquez, M., Hammett, G.W., Shi, E.L., 2020. Continuum electromagnetic gyrokinetic simulations of turbulence in the tokamak scrape-off layer and laboratory devices. *Physics of Plasmas* 27, 042304. doi:10.1063/1.5141157.
- [45] Hassan, E., Hatch, D., Halfmoon, M., Curie, M., Kotchenreuther, M., Mahajan, S., Merlo, G., Groebner, R., Nelson, A., Diallo, A., 2021. Identifying the microtearing modes in the pedestal of DIII-D H-modes using gyrokinetic simulations. *Nuclear Fusion* 62, 026008. doi:10.1088/1741-4326/ac3be5.
- [46] Hatch, D., Kotschenreuther, M., Li, P.Y., Chapman-Oplopoiou, B., Parisi, J., Mahajan, S., Groebner, R., 2024. Modeling electron temperature profiles in the pedestal with simple formulas for ETG transport. *Nuclear Fusion* 64, 066007. doi:10.1088/1741-4326/ad3972.
- [47] Hatch, D.R., Jenko, F., Bañón Navarro, A., Bratanov, V., 2013. Transition between Saturation Regimes of Gyrokinetic Turbulence. *Physical Review Letters* 111, 175001. doi:10.1103/PhysRevLett.111.175001.
- [48] Hatch, D.R., Michoski, C., Kuang, D., Chapman-Oplopoiou, B., Curie, M., Halfmoon, M., Hassan, E., Kotschenreuther, M., Mahajan, S.M., Merlo, G., Pueschel, M.J., Walker, J., Stephens, C.D., 2022. Reduced models for ETG transport in the tokamak pedestal. *Physics of Plasmas* 29, 062501. doi:10.1063/5.0087403.
- [49] Hernandez, V., Roman, J.E., Vidal, V., 2005. SLEPc: A scalable and flexible toolkit for the solution of eigenvalue problems. *ACM Transactions on Mathematical Software* 31, 351–362. doi:10.1145/1089014.1089019.
- [50] Huhn, Q.A., Tano, M.E., Ragusa, J.C., Choi, Y., 2023. Parametric dynamic mode decomposition for reduced order modeling. *Journal of Computational Physics* 475, 111852. doi:<https://doi.org/10.1016/j.jcp.2022.111852>.
- [51] Ichinaga, S.M., Andreuzzi, F., Demo, N., Tezzele, M., Lapo, K., Rozza, G., Brunton, S.L., Kutz, J.N., 2024. PyDMD: A Python Package for Robust Dynamic Mode Decomposition. *Journal of Machine Learning Research* 25, 1–9. URL: <http://jmlr.org/papers/v25/24-0739.html>.
- [52] Jantsch, P., Webster, C.G., Zhang, G., 2018. On the Lebesgue constant of weighted Leja points for

- Lagrange interpolation on unbounded domains. *IMA Journal of Numerical Analysis* 39, 1039–1057. doi:10.1093/imanum/dry002.
- [53] Jarema, D., Bungartz, H., Görler, T., Jenko, F., Neckel, T., Told, D., 2017. Block-structured grids in full velocity space for Eulerian gyrokinetic simulations. *Computer Physics Communications* 215, 49–62. doi:<https://doi.org/10.1016/j.cpc.2017.02.005>.
- [54] Jenko, F., Dorland, W., Kotschenreuther, M., Rogers, B.N., 2000. Electron temperature gradient driven turbulence. *Physics of Plasmas* 7, 1904–1910. doi:10.1063/1.874014.
- [55] Kammerer, M., Merz, F., Jenko, F., 2008. Exceptional points in linear gyrokinetics. *Physics of Plasmas* 15, 052102. doi:10.1063/1.2909618.
- [56] Kaptanoglu, A.A., Morgan, K.D., Hansen, C.J., Brunton, S.L., 2020. Characterizing Magnetized Plasmas with Dynamic Mode Decomposition. *Physics of Plasmas* 27, 032108. doi:10.1063/1.5138932.
- [57] Kleiber, R., Borchardt, M., Hatzky, R., Könies, A., Leyh, H., Mishchenko, A., Riemann, J., Slaby, C., na, J.G.R., Sánchez, E., Cole, M., 2024. EUTERPE: A global gyrokinetic code for stellarator geometry. *Computer Physics Communications* 295, 109013. doi:<https://doi.org/10.1016/j.cpc.2023.109013>.
- [58] Konrad, J., Farcaş, I.G., Peherstorfer, B., Di Siena, A., Jenko, F., Neckel, T., Bungartz, H.J., 2022. Data-driven low-fidelity models for multi-fidelity Monte Carlo sampling in plasma micro-turbulence analysis. *Journal of Computational Physics* 451, 110898. doi:<https://doi.org/10.1016/j.jcp.2021.110898>.
- [59] Kramer, B., Peherstorfer, B., Willcox, K.E., 2024. Learning Nonlinear Reduced Models from Data with Operator Inference. *Annual Review of Fluid Mechanics* 56, 521–548. doi:<https://doi.org/10.1146/annurev-fluid-121021-025220>.
- [60] Ku, S.H., Hager, R., Scheinberg, A., Dominski, J., Sharma, A., Churchill, M., Choi, J., Sturdevant, B., Mollén, A., Wilkie, G., Chang, C.S., Yoon, E., Adams, M., Seo, J., Koh, S., D’Azevedo, E., Abbott, S., Worley, P.H., Ethier, S., Park, G., Lang, J., MacKie-Mason, B., Germaschewski, K., Suchyta, E., Carey, V., Cole, M., Trivedi, P., Chowdhury, J., 2018. Xgc. [Computer Software] <https://doi.org/10.11578/dc.20180627.11>. doi:10.11578/dc.20180627.11.
- [61] Kutz, J.N., Brunton, S.L., Brunton, B.W., Proctor, J.L., 2016. *Dynamic Mode Decomposition*. Society for Industrial and Applied Mathematics, Philadelphia, PA. doi:10.1137/1.9781611974508.
- [62] Lanti, E., Ohana, N., Tronko, N., Hayward-Schneider, T., Bottino, A., McMillan, B., Mishchenko, A., Scheinberg, A., Biancalani, A., Angelino, P., Brunner, S., Dominski, J., Donnel, P., Gheller, C., Hatzky, R., Jocksch, A., Jolliet, S., Lu, Z., Collar, J.M., Novikau, I., Sonnendrücker, E., Vernay, T., Villard, L., 2020. Orb5: A global electromagnetic gyrokinetic code using the PIC approach in toroidal geometry. *Computer Physics Communications* 251, 107072. doi:<https://doi.org/10.1016/j.cpc.2019.107072>.
- [63] Lee, S., Jang, K., Lee, S., Cho, H., Shin, S., 2024. Parametric model order reduction by machine learning for fluid–structure interaction analysis. *Engineering with Computers* 40, 45–60. doi:10.1007/s00366-023-01782-2.
- [64] Lin, Z., Hahm, T.S., Lee, W.W., Tang, W.M., White, R.B., 1998. Turbulent Transport Reduction by Zonal Flows: Massively Parallel Simulations. *Science* 281, 1835–1837. doi:10.1126/science.281.5384.1835.
- [65] Maday, Y., Rønquist, E.M., 2002. A Reduced-Basis Element Method. *Journal of Scientific Computing* 17, 447–459. doi:10.1023/A:1015197908587.
- [66] Mandell, N., Dorland, W., Abel, I., Gaur, R., Kim, P., Martin, M., Qian, T., 2024. GX: a GPU-native gyrokinetic turbulence code for tokamak and stellarator design. *Journal of Plasma Physics* 90, 905900402. doi:10.1017/S0022377824000631.
- [67] McQuarrie, S.A., Khodabakhshi, P., Willcox, K.E., 2023. Nonintrusive Reduced-Order Models for Parametric Partial Differential Equations via Data-Driven Operator Inference. *SIAM Journal on Scientific Computing* 45, A1917–A1946. doi:10.1137/21M1452810.

- [68] Narayan, A., Jakeman, J.D., 2014. Adaptive Leja Sparse Grid Constructions for Stochastic Collocation and High-Dimensional Approximation. *SIAM Journal on Scientific Computing* 36, A2952–A2983. doi:10.1137/140966368.
- [69] Peherstorfer, B., Willcox, K., 2016. Data-driven operator inference for nonintrusive projection-based model reduction. *Computer Methods in Applied Mechanics and Engineering* 306, 196–215. doi:<https://doi.org/10.1016/j.cma.2016.03.025>.
- [70] Peherstorfer, B., Zimmer, S., Bungartz, H.J., 2013. Model Reduction with the Reduced Basis Method and Sparse Grids, in: Garcke, J., Griebel, M. (Eds.), *Sparse Grids and Applications*, Springer Berlin Heidelberg, Berlin, Heidelberg. pp. 223–242. doi:10.1007/978-3-642-31703-3_11.
- [71] Phuong Huynh, D.B., Knezevic, D.J., Patera, A.T., 2013. A Static condensation Reduced Basis Element method : approximation and *a posteriori* error estimation. *ESAIM: Mathematical Modelling and Numerical Analysis* 47, 213–251. doi:10.1051/m2an/2012022.
- [72] van de Plassche, K.L., Citrin, J., Bourdelle, C., Camenen, Y., Casson, F.J., Dagnelie, V.I., Felici, F., Ho, A., Van Mulders, S., Contributors, J., 2020. Fast modeling of turbulent transport in fusion plasmas using neural networks. *Physics of Plasmas* 27, 022310. doi:10.1063/1.5134126.
- [73] Pueschel, M.J., Faber, B.J., Citrin, J., Hegna, C.C., Terry, P.W., Hatch, D.R., 2016. Stellarator Turbulence: Subdominant Eigenmodes and Quasilinear Modeling. *Physical Review Letters* 116, 085001. doi:10.1103/PhysRevLett.116.085001.
- [74] Rajaram, D., Perron, C., Puranik, T.G., Mavris, D.N., 2020. Randomized Algorithms for Non-Intrusive Parametric Reduced Order Modeling. *AIAA Journal* 58, 5389–5407. doi:10.2514/1.J059616.
- [75] Renganathan, S.A., 2020. Koopman-Based Approach to Nonintrusive Reduced Order Modeling: Application to Aerodynamic Shape Optimization and Uncertainty Propagation. *AIAA Journal* 58, 2221–2235. doi:10.2514/1.J058744.
- [76] Renganathan, S.A., Maulik, R., Rao, V., 2020. Machine learning for nonintrusive model order reduction of the parametric inviscid transonic flow past an airfoil. *Physics of Fluids* 32, 047110. doi:10.1063/1.5144661.
- [77] Rodriguez-Fernandez, P., Howard, N., Candy, J., 2022. Nonlinear gyrokinetic predictions of SPARC burning plasma profiles enabled by surrogate modeling. *Nuclear Fusion* 62, 076036. doi:10.1088/1741-4326/ac64b2.
- [78] Romero, E., Roman, J.E., 2014. A parallel implementation of Davidson methods for large-scale eigenvalue problems in SLEPc. *ACM Transactions on Mathematical Software* 40. doi:10.1145/2543696.
- [79] ROWLEY, C.W., MEZIĆ, I., BAGHERI, S., SCHLATTER, P., HENNINGSON, D.S., 2009. Spectral analysis of nonlinear flows. *Journal of Fluid Mechanics* 641, 115–127. doi:10.1017/S0022112009992059.
- [80] Schmid, P.J., 2010. Dynamic mode decomposition of numerical and experimental data. *Journal of Fluid Mechanics* 656, 5–28. doi:10.1017/S0022112010001217.
- [81] Sina Brunsch, 2017. Parametric Model Order Reduction Using Sparse Grids. Ph.D. thesis. Rheinische Friedrich-Wilhelms-Universität Bonn. URL: <https://hdl.handle.net/20.500.11811/7247>.
- [82] Taylor, R., Kutz, J.N., Morgan, K., Nelson, B.A., 2018. Dynamic mode decomposition for plasma diagnostics and validation. *Review of Scientific Instruments* 89, 053501. doi:10.1063/1.5027419.
- [83] Terry, P.W., Baver, D.A., Gupta, S., 2006. Role of stable eigenmodes in saturated local plasma turbulence. *Physics of Plasmas* 13, 022307. doi:10.1063/1.2168453.
- [84] Tu, J.H., Rowley, C.W., Luchtenburg, D.M., Brunton, S.L., Kutz, J.N., 2014. On dynamic mode decomposition: Theory and applications. *Journal of Computational Dynamics* 1, 391–421.
- [85] Wagner, F., Becker, G., Behringer, K., Campbell, D., Eberhagen, A., Engelhardt, W., Fussmann, G., Gehre, O., Gernhardt, J., Gierke, G.v., Haas, G., Huang, M., Karger, F., Keilhacker, M., Klüber, O., Kornherr, M., Lackner, K., Lisitano, G., Lister, G.G., Mayer, H.M., Meisel, D., Müller, E.R., Murmann, H., Niedermeyer, H., Poschenrieder, W., Rapp, H., Röhr, H., Schneider, F., Siller, G., Speth, E., Stäbler,

- A., Steuer, K.H., Venus, G., Vollmer, O., Yü, Z., 1982. Regime of Improved Confinement and High Beta in Neutral-Beam-Heated Divertor Discharges of the ASDEX Tokamak. *Physical Review Letters* 49, 1408–1412. doi:10.1103/PhysRevLett.49.1408.
- [86] Walker, J., Hatch, D.R., 2023. ETG turbulence in a tokamak pedestal. *Physics of Plasmas* 30, 082307. doi:10.1063/5.0146968.
- [87] Watanabe, T.H., Sugama, H., 2005. Velocity–space structures of distribution function in toroidal ion temperature gradient turbulence. *Nuclear Fusion* 46, 24. doi:10.1088/0029-5515/46/1/003.
- [88] Whelan, G.G., Pueschel, M.J., Terry, P.W., 2018. Nonlinear Electromagnetic Stabilization of Plasma Microturbulence. *Physical Review Letters* 120, 175002. doi:10.1103/PhysRevLett.120.175002.
- [89] Xanthopoulos, P., Cooper, W.A., Jenko, F., Turkin, Y., Runov, A., Geiger, J., 2009. A geometry interface for gyrokinetic microturbulence investigations in toroidal configurations. *Physics of Plasmas* 16, 082303. doi:10.1063/1.3187907.
- [90] Xiao, D., Lin, Z., Fang, F., Pain, C.C., Navon, I.M., Salinas, P., Muggeridge, A., 2017. Non-intrusive reduced-order modeling for multiphase porous media flows using Smolyak sparse grids. *International Journal for Numerical Methods in Fluids* 83, 205–219. doi:https://doi.org/10.1002/flid.4263.
- [91] Yoshida, M., McDermott, R., Angioni, C., Camenen, Y., Citrin, J., Jakubowski, M., Hughes, J., Idomura, Y., Mantica, P., Mariani, A., Mordijck, S., Paul, E., Tala, T., Verdoolaege, G., Zocco, A., Casson, F., Dif-Pradalier, G., Duval, B., Grierson, B., Kaye, S., Manas, P., Maslov, M., Odstrcil, T., Rice, J., Schmitz, L., Sciortino, F., Solano, E., Staebler, G., Valovič, M., Wolfrum, E., Snipes, J., the Transport, Group, C., 2025. Transport and confinement physics: Chapter 2 of the special issue: on the path to tokamak burning plasma operation. *Nuclear Fusion* 65, 033001. doi:10.1088/1741-4326/ad8ced.
- [92] Zahr, M.J., Carlberg, K.T., Kouri, D.P., 2019. An Efficient, Globally Convergent Method for Optimization Under Uncertainty Using Adaptive Model Reduction and Sparse Grids. *SIAM/ASA Journal on Uncertainty Quantification* 7, 877–912. doi:10.1137/18M1220996.